An Analysis of Frontogenesis in Numerical Simulations of Baroclinic Waves

RICHARD ROTUNNO, WILLIAM C. SKAMAROCK, AND CHRIS SNYDER

National Center for Atmospheric Research, * *Boulder, Colorado*

(Manuscript received 10 September 1993, in final form 17 January 1994)

ABSTRACT

Using a primitive equation (PE) model, we revisit two canonical flows that were previously studied using a semigeostrophic equation (SG) model. In a previous paper, the authors showed that the PE and the SG models can have significantly different versions of the large-scale dynamics—here they report on the implications of this difference for frontogenesis. The program for the study of frontogenesis developed by B. J. Hoskins and collaborators is followed to show how, in the PE version of the canonical cases, the surface warm front develops before the cold front, and why the upper-level front is a long, nearly continuous feature going from ridge to trough. The frontogenesis experienced by an air parcel is computed following the parcel to illustrate better the mechanisms involved. As the present calculations are carried out longer than most previous ones, the relation of the upper frontogenesis to the formation of the upper-level "cutoff" cyclone is also examined. Trajectory and three-dimensional graphical analyses show, with respect to the latter, the extreme distortions of the isentropic surfaces and mixing-induced variations in the potential vorticity field.

1. Introduction

The basic idea in the modern theory of frontogenesis is that a geostrophically induced increase in the magnitude of the horizontal temperature gradient, $|\nabla_H \theta|$, gives rise to an ageostrophic circulation that tends to increase $|\nabla_H \theta|$ even further (Hoskins and Bretherton 1972, hereafter HB; Hoskins 1982). The $|\nabla_H \theta|$-increasing geostrophic winds were given in HB by simple deformation fields that allowed for two-dimensional solutions representing infinitely long fronts. Later work by Hoskins and West (1979, hereafter HW), using a three-dimensional semigeostrophic (SG) model, examined frontogenesis within an evolving baroclinic wave. In that model the $|\nabla_H \theta|$-increasing geostrophic winds are those that develop in the course of wave development. Frontogenesis occurs in the sectors of the wave where the forcing of the frontogenesis is strong, *and* where air parcel trajectories are such that the parcels reside for a sufficient time in those sectors (Hoskins 1982, p. 146). As shown in HW, both of these factors depend on the structure of the baroclinic wave, which in turn depends on physical factors such as the particular meridional shear of the base state. It has been recently shown (Snyder et al. 1991, hereafter SSR) that the structure of a numerically simulated baroclinic

wave is affected significantly by the SG approximation. In view of this, we have used a primitive equation (PE) model to reexamine the canonical case studies of frontogenesis of HW (SG model of a constant-potential-vorticity jet in a troposphere bounded above by a "lid") and of Heckley and Hoskins [(1982, hereafter HH), where the lid is removed and replaced by a constant-potential-vorticity stratosphere].

We select two simulations for detailed study here. In SSR, the HW case was simulated with our PE model. Heckley and Hoskins extended HW to include a stratosphere, and, accordingly, we have now simulated the HH case with our PE model. In the course of analyzing these results we noted some qualitative differences with respect to simulations of upper-level frontogenesis in other studies (Buzzi et al. 1977; Newton and Trevisan 1984; Keyser et al. 1989). We determined that most of the difference is due to the use of a jet in HH of strength ~ 30 m s^{-1}, whereas the others used much stronger jets (60–80 m s^{-1}). The direct effect of the stronger jet is that the vertical velocities in the evolving wave are much stronger (and closer to observed values) and, consequently, play a different role in the upper frontogenesis. Therefore, we analyze simulations designated HH70 (HH, but with a 70 m s^{-1} jet), and for comparison with the latter, HW60 (HW, but with a 60 m s^{-1} jet). Results from our simulation of the HH case will be discussed only briefly to describe how the weaker vertical motion field changes the character of the simulated upper-level frontogenesis.

The program we follow is as prescribed by Hoskins (1982). First, the forcing of frontogenesis by the geostrophic wind is diagnosed in terms of the Q vector

(Hoskins et al. 1978). Second, the pattern of **Q** gives an estimate of the three-dimensional ageostrophic wind, which together with the θ field allows an estimation of the forcing of frontogenesis due to the ageostrophic wind. If the ageostrophic effect reinforces the geostrophic, a positive feedback is at work. Finally, one examines the history of air parcels that flow through the regions of frontogenesis to see whether they spend sufficient time in those regions to form a significant front. We refer to these steps below simply as "the program."

We begin with an analysis of surface frontogenesis in HW60; HW (p. 1677) show that the frontogenesis is sensitive to the meridional phase tilt of the geopotential wave. As demonstrated in SSR's PE simulation of the HW $\mu = 1$ case, the geopotential wave has a much more pronounced northwest–southeast (NW–SE) tilt than it does in the SG simulation. Following the program, we show how this tilt leads to the tendency for warm frontogenesis to occur before cold frontogenesis in the present PE simulations. Later in the baroclinic wave life cycle, the warm frontogenesis slows, while the cold frontogenesis intensifies; we identify this with the drastic change in flow topology that occurs when the temperature wave at the surface "breaks."

In the case of upper frontogenesis, the situation is more complex; to gain some intuition we look first at the upper front produced at the lid in HW60. Following the program, we show how the NW–SE tilt in the geopotential wave leads to a front at the lid that runs NW to SE from the ridge to the trough. With the lid, the frontogenesis is effected by ageostrophic flow that is in response to the geostrophic forcing of frontogenesis. When the lid is removed in the HH70 case, the ageostrophic response to the geostrophic forcing of frontogenesis can produce frontogenesis through "tilting" of the strong vertically oriented potential temperature gradient of the stratosphere to the horizontal by vertical motions (see Keyser and Shapiro 1986, section 2). Our analysis shows that both confluence and tilting are at work in the HH70 case when the baroclinic wave reaches large amplitude: near and just downstream of the ridge, there is frontogenesis mainly through horizontal flow confluence (as in HW60). Farther downstream, but just upstream of the trough, the strong vertical motions increase $|\nabla_H \theta|$ through tilting. With both effects at work along different segments of the flow, a long upper front is obtained that extends from ridge to trough.

The upper-level frontogenesis is intimately associated with the development of an upper-level cutoff cyclone, at least in flow situations studied here. We examine the complex flow topology at the large amplitude stage through a variety of graphical devices. This analysis shows the extreme deformations experienced by the isentropic surfaces during cutoff development and

the complexity of the three-dimensional stirring process that the cutoff signifies.

In SSR, we compared the PE and SG versions of the large-scale dynamics of baroclinic waves for a base state with constant potential vorticity (PV) bounded above by a lid. Here we continue with a study of how the large-scale PE dynamics affects the embedded frontogenesis in that case, and in another case where the tropopause is treated more realistically. Our strategy is to use the insights offered by the SG studies as a point of reference but to retain the more accurate PE dynamics. With this approach, we hope to produce an analysis that better connects the PE results to our basic theoretical notions of frontogenesis. Although this study is limited to the flow in an f-plane channel, the success of the present approach suggests that it could be used to good advantage in more general flow geometries.

2. Tools for analyzing frontogenesis

In three-dimensional synoptic-scale flow, both quasigeostrophic (QG) and SG theory have errors that are $O(\text{Ro})$, where Ro is the Rossby number, compared to the PE (McWilliams and Gent 1980). SSR have shown how these small errors accumulate to produce systematic differences in PE and SG solutions. Near fronts, a different scaling is appropriate (HB, McWilliams and Gent 1980), and SG has at least leading-order accuracy, while QG makes errors that are formally $O(1)$.

Nevertheless, our basic point of reference for the present analysis is quasigeostrophic theory. There are two reasons for this, which relate to the desire for both accuracy and clarity. With respect to clarity, QG theory is both familiar and simple. With respect to accuracy, if one applies a QG diagnosis to the PE solutions at any given time, there is only the small $O(\text{Ro})$ error between them at that time. Of course, the errors in the QG diagnosis may be locally larger near fronts or other intense features. Even then, however, our experience is that inferences based on QG theory often remain qualitatively useful [see Keyser et al. (1992, hereafter KSD) for further discussion of this point].

The following summary of the QG framework is based on the recent essay by Davies-Jones (1991). In the Boussinesq QG limit, the equations for $\nabla_H \theta$ and the horizontal geostrophic vorticity ω_H are, respectively,

$$\frac{g}{\theta_0} d_g \nabla_H \theta = \frac{g}{\theta_0} \mathbf{Q} - N^2 \nabla_H w \qquad (1)$$

and

$$f d_g \omega_H = \frac{g}{\theta_0} \mathbf{Q} + f^2 \partial_z \mathbf{u}_a, \qquad (2)$$

where

$$\mathbf{Q} = (Q^x, Q^y)$$

$$= -(\partial_x u_g \partial_x \theta + \partial_x v_g \partial_y \theta, \ \partial_y u_g \partial_x \theta + \partial_y v_g \partial_y \theta) \qquad (3)$$

is the vector introduced by Hoskins et al. (1978), $(u_g, v_g) = f^{-1}(-\partial_y\phi, \partial_x\phi)$ is the geostrophic velocity, $(\mathbf{u}_a, w)$ is the ageostrophic velocity, and $d_g = \partial_t + u_g\partial_x + v_g\partial_y$. The thermal wind relation is $f\omega_H = -\theta_0^{-1}g\nabla\theta$; from (1) and (2) it is easy to see that geostrophic motion alone would tend to change $f\omega_H$ and $-\theta_0^{-1}g\nabla\theta$ by equal amounts in opposite directions, destroying thermal wind balance. The ageostrophic motions that would allow thermal wind balance to continue in the face of the geostrophically induced changes represented by $\mathbf{Q}$ are governed by (1) + (2):

$$N^2\nabla_H w - f^2\partial_z\mathbf{u}_a = 2\frac{g}{\theta_0}\mathbf{Q}. \qquad (4)$$

This equation[1] suggests a circulation in the vertical plane with rising motion at the head and sinking at the tail of the $\mathbf{Q}$ vector.

The simplest example of how to use (1)–(4) is the so-called deformation-induced front. Consider a field $\theta = \theta(x, z)$ with $\nabla\theta > 0$, subjected to a uniform geostrophic deformation $(u_g, v_g) = (-\alpha x, \alpha y)$, where $\alpha > 0$; by (3), $Q^x = \alpha\partial_x\theta > 0$ and $Q^y = 0$. One envisions that an air parcel moving inward toward $x = 0$ first experiences a geostrophic increase in $\partial_x\theta$ by the first term on the rhs of (1); however by (4), a direct (warm air rising/cold air sinking) ageostrophic circulation is set into motion that, by the second term on the rhs of (1), tends to tilt the isotherms toward the horizontal and thereby decrease $\partial_x\theta$. At a rigid horizontal boundary (the ground, say), the second term on the rhs of (1) is zero, and so the ageostrophic circulation has no effect on $\partial_x\theta$ there, at least at the QG level of approximation. Frontogenesis at the surface proceeds exponentially at a rate given by α.

In the theory of HB, the effect of the ageostrophic cross-front wind is included in the equation for $\partial_x\theta$; at the ground in the simple example it is

$$[\partial_t + (u_g + u_a)\partial_x]\partial_x\theta = Q^x - \partial_x u_a\partial_x\theta. \qquad (5)$$

A direct ageostrophic circulation has two effects in (5). First, $\partial_x u_a < 0$ on the warm side of $\partial_x\theta$ and so $-\partial_x u_a\partial_x\theta$ reinforces Q^x there. Second, since u_a opposes u_g in the same vicinity, air parcels reside for a long time in a place where the forcing is enhanced and, in this way, the ageostrophic effects reinforce the original geostrophically induced increase in $\partial_x\theta$. Thus, a positive feedback loop is described that implies a faster-than-exponential approach to a frontal singularity (i.e., $\partial_x\theta \to \infty$ in a finite time).

In the HB deformation front paradigm, the positive feedback idea is the central one—approximations such

as the restriction to purely two-dimensional flow are expedients that allow the basic idea to be exposed more clearly. Motivated by the positive feedback idea, but faced with more complex flow situations, we will proceed as follows with the analysis of our numerical simulations. The study of frontogenesis is a study of how $\nabla_H\theta\cdot\nabla_H\theta$ increases; the general form of (1) dotted with $\nabla_H\theta$ is

$$\frac{1}{2}d(\nabla_H\theta\cdot\nabla_H\theta) = \mathscr{F}_g + \mathscr{F}_a + \mathscr{F}_{\text{tilt}} = \mathscr{F}, \qquad (6)$$

where

$$\mathscr{F}_g = \mathbf{Q}\cdot\nabla_H\theta, \qquad (7)$$

$$\mathscr{F}_a = \mathbf{Q}_a\cdot\nabla_H\theta, \qquad (8)$$

$$\mathscr{F}_{\text{tilt}} = -(\nabla_H w\cdot\nabla_H\theta)\partial_z\theta, \qquad (9)$$

and where $\mathbf{Q}_a$ is defined as in (3), except u_a is substituted for u_g; d is the time rate of change following an air parcel moving with the full velocity (cf. section 5a of HW). With these equations, we can follow the program described in section 1: First, we compute $\mathbf{Q}$ to determine the geostrophically induced changes to $\nabla_H\theta$. Second, we infer qualitatively the ageostrophic flow through (4). Third, to assess whether there is a positive feedback, we measure the effect of the ageostrophic flow on frontogenesis through (8) and (9). Finally, we calculate the $\mathscr{F}$'s for air parcels taking part in the frontogenesis as they move through the flow field.

One potential weak point in the program is that (4) gives only a qualitative estimate of $(\mathbf{u}_a, w)$. The points we wish to make in the following depend only on the general pattern of $(\mathbf{u}_a, w)$, which in most instances can be reliably inferred from (4). The recent relevant study by KSD will be referred to as needed.

3. Constant-potential-vorticity jet troposphere under a lid

a. Initial state and large-scale flow evolution

The first case for study is designated HW60. The initial state, shown in Fig. 1, is the constant-potential-vorticity jet troposphere under a lid studied in HW (with $\mu = 1$), except here the maximum wind in the jet is 60 m s^{-1}, instead of the 30 m s^{-1} used in HW (and in SSR). The reason for using a stronger jet is described in section 4.

The PE model used in the present study is described in SSR (sections 2 and 3). A few of the salient features of the model are that the model is dry, Boussinesq, adiabatic, and inviscid save for a ∇^4 diffusion term.[2] The boundary conditions are that the flow is periodic

---

[1] Another important reason for using the QG system is that trying to improve the asymptotic accuracy of (4) by including terms of higher order in Ro would (alas) bring terms involving time derivatives, destroying its simple contemporaneous nature.

[2] In SSR, the diffusion was turned on starting at day 5 to achieve the least ambiguous comparison of inviscid PE to inviscid SG.
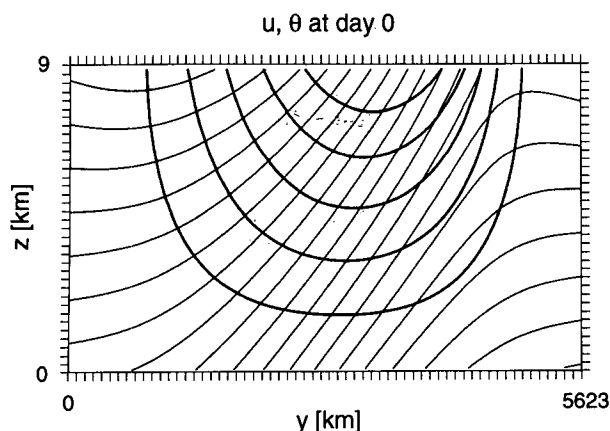
u, θ at day 0

FIG. 1. Zonal velocity [heavy contours, contour interval (CI) = 10 m s^{-1}] and potential temperature (lighter contours, CI = 5 K) for the HW constant-PV jet troposphere with $\mu = 1$. For this study, the maximum velocity in the jet is 60 m s^{-1} (in HW, a 30 m s^{-1} jet was used). Grid intervals are indicated by the tick marks.

in the x direction, $v = 0$ at the meridional boundaries, and $w = 0$ at the horizontal bounding surfaces. The domain of integration for HW60 is as in HW: $y_L = 5623$ km, $x_L = 4090$ km, and $H = 9$ km. For this Boussinesq model, PV $= \rho_0^{-1} \boldsymbol{\omega} \cdot \nabla \theta$, where $\rho_0 = 1$ kg m^{-3}; following Hoskins et al. (1985) we give PV here in terms of the PV unit (PVU) of 10^{-6} m^2 s^{-1} K kg^{-1}. In the base state shown in Fig. 1, the PV is constant and approximately 0.4 PVU; the Coriolis parameter $f = 10^{-4}$ s^{-1} and is also taken to be a constant. The x, y, and z directions are covered respectively by 41, 61, and 36 grid intervals so that $(\Delta x, \Delta y, \Delta z) = (99.8, 92.1, .25$ km$)$.

The most unstable normal mode grows with a doubling time of ~ 0.7 d (roughly half that reported in SSR, since the jet speed is doubled) and has a phase speed of 22 m s^{-1}. The mode's structure is illustrated in Fig. 2a by the perturbation geopotential field, ϕ', shown at the "surface" (lowest grid level, $\Delta z/2$), and at the "lid" (uppermost grid level, $H - \Delta z/2$). In addition to the usual westward phase tilt with height (for baroclinic instability) and northward phase tilt with height (the tendency of the mode to follow the northward slanting surfaces of constant absolute momentum predicted by SG theory), there is a northward displacement of the maximum amplitude of the mode to the cyclonic shear side of the jet. The latter feature, which does not occur in the SG simulation (Fig. 2b), was shown in SSR to be due to $O(\text{Ro}^2)$ terms not contained in SG. Since Ro is larger here, these differences between PE and SG are even more pronounced than they were for the HW case studied in SSR.

The reason for the meridional phase tilt in the x–y plane of the unstable mode is a matter of some subtlety, even in a QG model (which would suffice to produce the basic horizontal phase variation shown in Fig. 2b). Held and Andrews (1983) found, through a series of

computations for a variety of cases using QG theory, that the vertically integrated meridional momentum flux will in most cases be upgradient (and hence the meridional phase tilt will be "with the shear" on average) if the meridional scale of the jet is on the order of, or larger than, $NH/f(\sim 1000$ km in the present case). Since the meridional scale of the jet shown in Fig. 1 is $5623/2\pi$ km, the Held–Andrews rule predicts that the basic phase tilt of the unstable mode should be with the shear; this is consistent with the patterns shown in Fig. 2. Also, HW (p. 1667) noted the more pronounced phase tilt near the jet edges where there are critical lines (see also Davies et al. 1991). Now, neither QG nor SG accounts for the strong NW–SE asymmetry
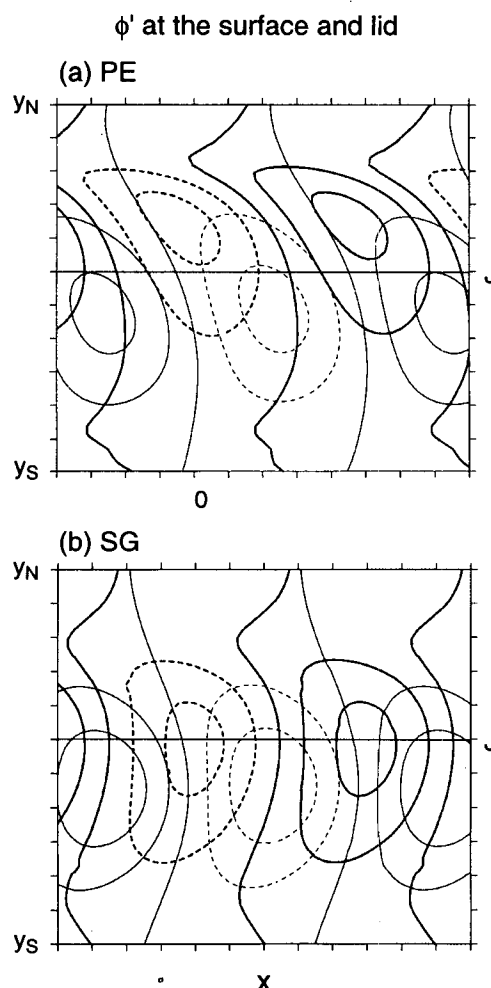
φ' at the surface and lid

(a) PE

(b) SG

FIG. 2. The perturbation geopotential ϕ' for the most unstable normal mode of the jet shown in Fig. 1 at the lid (heavy contours) and at the surface (light contours) for the (a) PE model and (b) SG model. Dashed contours indicate negative values. The contour interval for each model is 2/5 of the (arbitrary) mode amplitude. In the north–south direction only a portion of the domain is shown ($y_S = 1000$ km, $y_N = 5500$ km); in the east–west direction $1.2 \times x_L$ is shown. Here and in subsequent figures the tick marks are spaced $0.1x_L(\sim 409)$ km apart in both directions. Jet axis at the lid is indicated.

of the PE mode; in SSR an argument was given (pp. 2190–2191) for why the amplitude of the PE mode is shifted toward the north (cyclonic shear) side of the jet that accounts for some (but not all) of the NW–SE bias seen in Fig. 2a.

The integrations of the PE model are begun (day 0) as in SSR by setting the amplitude of the geopotential wave such that the meridional velocity maximum is 1.7 m s^{-1} at the surface. Figures 3–4 show the development of the potential temperature θ (or simply "temperature" hereafter) and geopotential ϕ at the surface and at the lid, respectively, at days 0, 4, 5, and 5.5 (the perturbation away from the initial state ϕ' is shown at day 0 at the lid for clarity).

Consider the development at the surface from day 0 to day 4. Two weak nonlinear features are in evidence. First, there is a northwestward relative drift of the lows and a southeastward relative drift of the highs. From potential vorticity arguments (Hoskins et al. 1985), the westward phase tilt with height of ϕ' and the NW–SE bias of ϕ' clearly imply this behavior. The second feature is that the elliptically shaped low has its major axis cyclonically rotated toward the x axis, while the elliptically shaped high has its major axis rotated anticyclonically toward the y axis. This behavior is due to shape of the mode. The NW–SE tilt of the elliptical pattern of ϕ implies an even more strongly tilted elliptical pattern of geostrophic vorticity[3]; geostrophic advection of this geostrophic vorticity pattern acts to rotate the major axis of the positive vorticity ellipse cyclonically toward the x axis, whereas the major axis of the negative vorticity ellipse is rotated anticyclonically toward the y axis.

Near and beyond day 4 further nonlinear effects may be identified as the modified mean flow (implied by the first two mechanisms mentioned above) interacts with the perturbations from the mean. A complete study of the chain of events that takes the wave to the point of breaking is beyond the scope of the present study.[4] However, it seems safe to say that the stretching of relative vorticity has become an important effect by day 4. [An analysis of the vorticity indicates that by day 4, $(\zeta_{max}, \zeta_{min}) \approx [1.2, -0.4]f$; by day 5, $(\zeta_{max}, \zeta_{min}) \approx (5, -0.75]f$.] From day 0 to day 5, the warm front (enhanced temperature gradient NE of the low) is a stronger feature than the cold front (enhanced temperature gradient SW of the low).

At the lid (Fig. 4) the lows (highs) drift southeastward (northwestward) for the same reason as alluded to above for the motion of the surface features. Since the wave-relative flow speed is larger at the lid than at the surface, and the amplitude of ϕ' is about the same,

the meridional particle displacements are smaller (Whitaker and Snyder 1993). The effect described above relating to the shape of ϕ' is small compared to the vorticity advection by the mean shear flow. Finally, as at the surface, the effects of vortex stretching at the lid are in evidence by day 4. With respect to frontogenesis, there is only one front that extends NW–SE from the ridge to the trough.

Just after day 5, the temperature wave "breaks" both at the surface and at the lid (Figs. 3d, 4d). At the surface, the warm front develops no further, while the cold front continues to intensify. At the lid, the NW–SE front extends from the ridge to the base of the trough.

b. Analysis of frontogenesis at the surface

At the outset of the simulation, the wave amplitude is small, and (3) can be linearized about the initial state, $\bar{\theta}(y, z)$, $\bar{u}(y, z)$, yielding

$$\mathbf{Q} \approx -\partial_y\bar{\theta}\nabla_H v_g' - \partial_y\bar{u}_g\partial_x\theta' \mathbf{j}, \qquad (10)$$

where primed variables represent departures from the initial state. Figure 3a shows $\mathbf{Q}$ at the surface at $t = 0$. In the present case, the second term on the rhs of (10) is zero at the surface; since $-\partial_y\bar{\theta} > 0$, $\mathbf{Q}$ simply points in the direction of increasing v_g'. The physical interpretation of these fields in the normal mode is simple. Consider $\mathbf{Q}$ near the low in Fig. 3a: $\mathbf{Q}$ points eastward over the low since the southward-pointing $\partial_y\bar{\theta}\mathbf{j}$ is being rotated eastward [see Fig. 2a of Hoskins et al. (1978)]. The north–south component of $\mathbf{Q}$ is due to the packing ($Q^y < 0$) or unpacking ($Q^y > 0$) together of the isotherms by v_g' [see Fig. 2b of Hoskins et al. (1978)]. Since ϕ is elliptically shaped and tilted NW–SE, $\partial_y v_g' > 0$ at the center of the low, and so $Q^y > 0$ there.[5] Figure 5 shows $\mathcal{F}_g$ and $\mathcal{F}_a$ at the surface at days 0, 4, 5, and 5.5 ($\mathcal{F}_{tilt} = 0$ at the surface and the lid) on the subdomains indicated in Fig. 3. Geostrophic frontogenesis occurs where $\mathbf{Q}$ points toward warm air; in the linear approximation this is where $Q^y < 0$. Figure 5a shows two regions of geostrophic frontogenesis: warm frontogenesis NE of the low, and cold frontogenesis to the SW. Due to the NW–SE modal tilt, the regions of geostrophic frontogenesis are also so tilted. So is, moreover, the convergence line of the $\mathbf{Q}$ vectors, which by (4) indicates ageostrophic flow toward that line; the ageostrophic frontogenesis shown in Fig. 5a is consistent with (4). Thus, the geostrophic frontogenesis along a NW–SE oriented line situated NE of the low gives rises to an ageostrophic flow that reinforces the former in the vicinity of that line.

As the unstable wave grows, the basic pattern at day 0 remains in evidence at day 4 (Figs. 3b, 5b). The most

---

[3] Consider the function $\phi = \frac{1}{2}(1 + \cos y)\sin(x + y/2)$, $x \in (0, 2\pi)$, $y \in (-\pi, \pi)$, which resembles the mode shown in Fig. 2a.

[4] See, for example, Nakamura (1993) or Thorncroft et al. (1993) for current ideas on how this development occurs.

[5] If ϕ were circularly shaped, $\mathbf{Q}$ would point along the isotherms at the center of the low (see Keyser et al. 1988, Fig. 10a); in the linear approximation, therefore, Q^y would be ≈ 0.

φ, θ, **Q** at the surface

(a) day 0

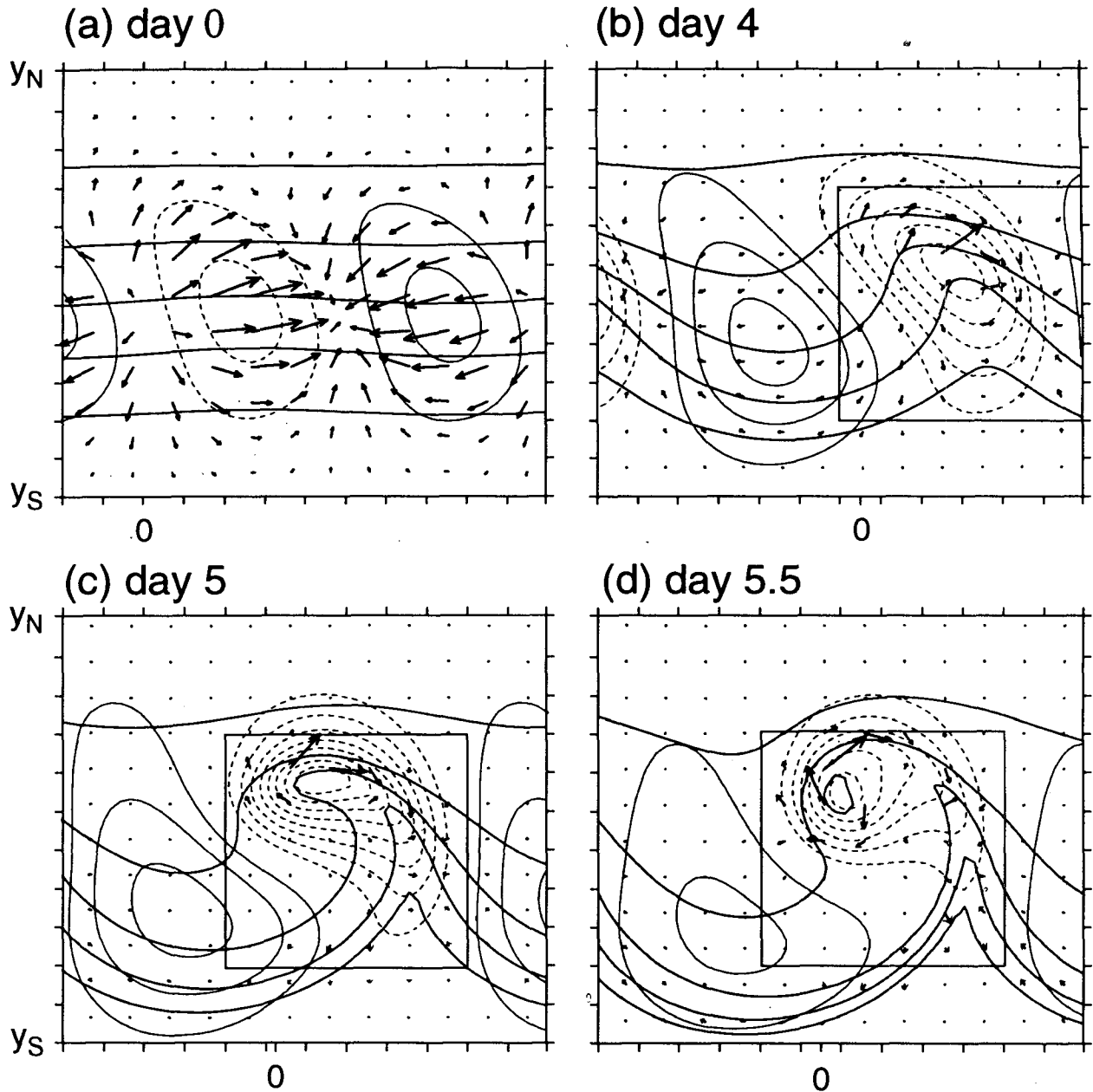## (b) day 4

(c) day 5

(d) day 5.5

FIG. 3. Time sequence of θ (heavy contours, CI = 10 K), ϕ (light contours; dashed contours indicate negative values; zero contours omitted here and in all subsequent contour plots), and **Q** at the surface at (a) day 0, ϕ CI = 40 m² s⁻², (b) day 4, ϕ CI = 300 m² s⁻², (c) day 5, ϕ CI = 500 m² s⁻², and (d) day 5.5, ϕ CI = 1000 m² s⁻². The scaling for **Q** varies from panel to panel and is chosen for clarity of presentation—the units are not important to the discussion; the vector is plotted only at every fourth grid point. The display domain in the east–west direction is 1.2 × x_L; the $x = 0$ point is assigned to the phase of the wave indicated in Fig. 2 and translated at the wave speed (22 m s⁻¹) for the subsequent display times; y_S and y_N are as in Fig. 2. Subdomains used for analysis in Fig. 5 are indicated in (b)–(d).

striking change in **Q** and $\mathscr{F}_g$ is the indication of stronger geostrophic frontolysis near the center of the low. As explained above, the elliptical shape with NW–

SE tilt of ϕ implies a frontolytical deformation field at the low center. As the area of low ϕ contracts in scale and becomes stronger, while retaining its tilted ellipti-

ϕ, θ, **Q** at the lid

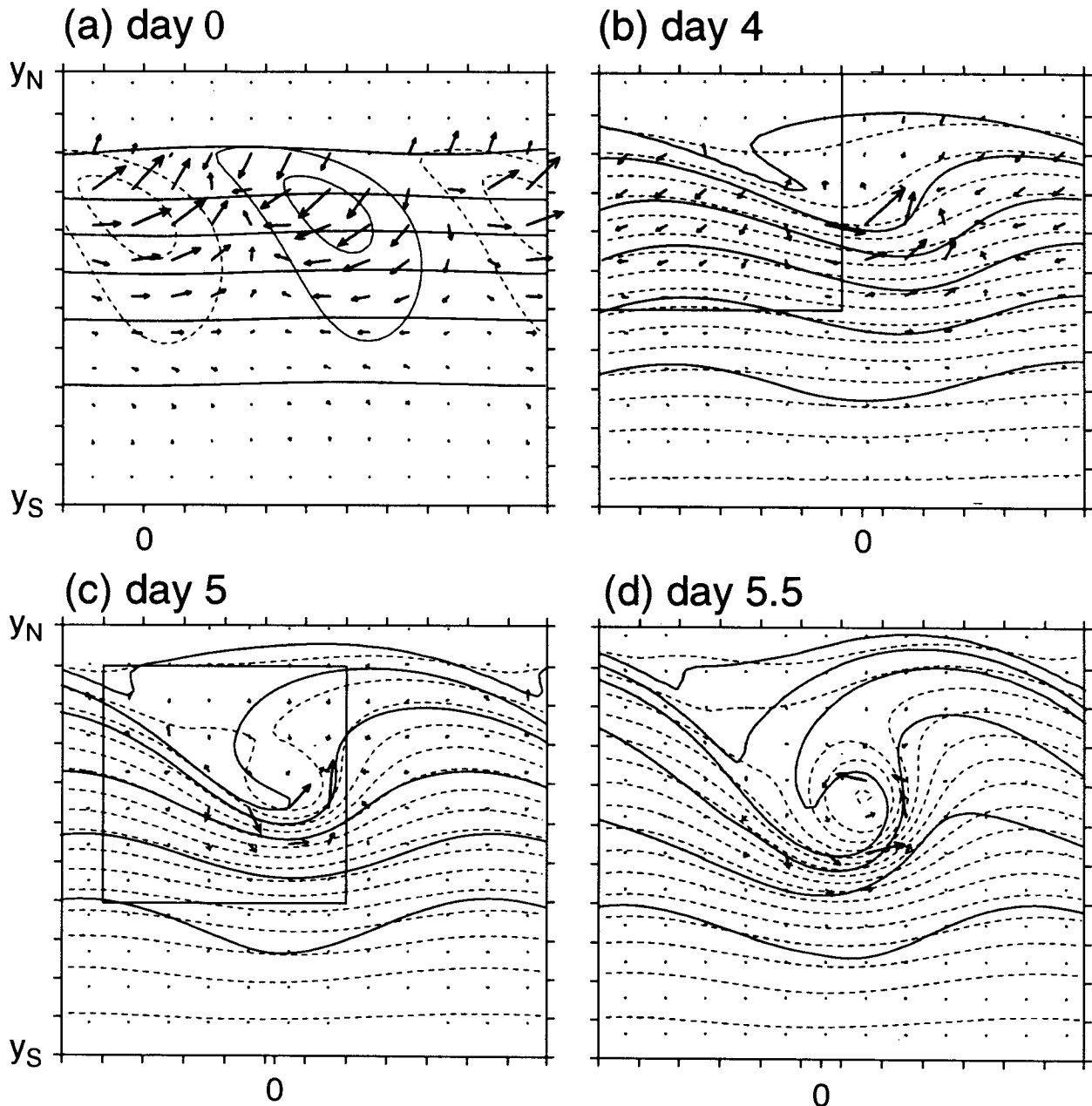## (a) day 0

(b) day 4

(c) day 5

(d) day 5.5

FIG. 4. As in Fig. 3 except at the lid. At the lid, the ϕ field reflects the large base-state velocity there; contour lines are dashed and plotted at intervals of 1000 m^2 s^{-2}, decreasing toward the north. In (a), ϕ' (CI: 40 m^2 s^{-2}) is plotted for clarity. Subdomains used for analysis in Fig. 8 are indicated in (b) and (c).

cal shape, the frontolytical deformation grows larger. Since $\mathbf{u}_a \sim \mathbf{Q}$, and since $\nabla_H \theta$ is increasing NE of the low and decreasing SW, $\mathscr{F}_a$ (Fig. 5b) also develops a large bias toward frontogenesis. The picture of warm frontogenesis that emerges is basically as described for the mode in Fig. 5a: there is a pattern of $\mathscr{F}_g < 0$ near

the low center and $\mathscr{F}_g > 0$ to the NE; this implies ageostrophic confluence and $\mathscr{F}_a > 0$ along the NW–SE line where $\mathscr{F}_g \approx 0$. This basic picture holds even as the warm front evolves toward smaller scales, as shown in Figs. 5c,d. By day 4, the perturbation wind speed at the surface is about half as large as the wave
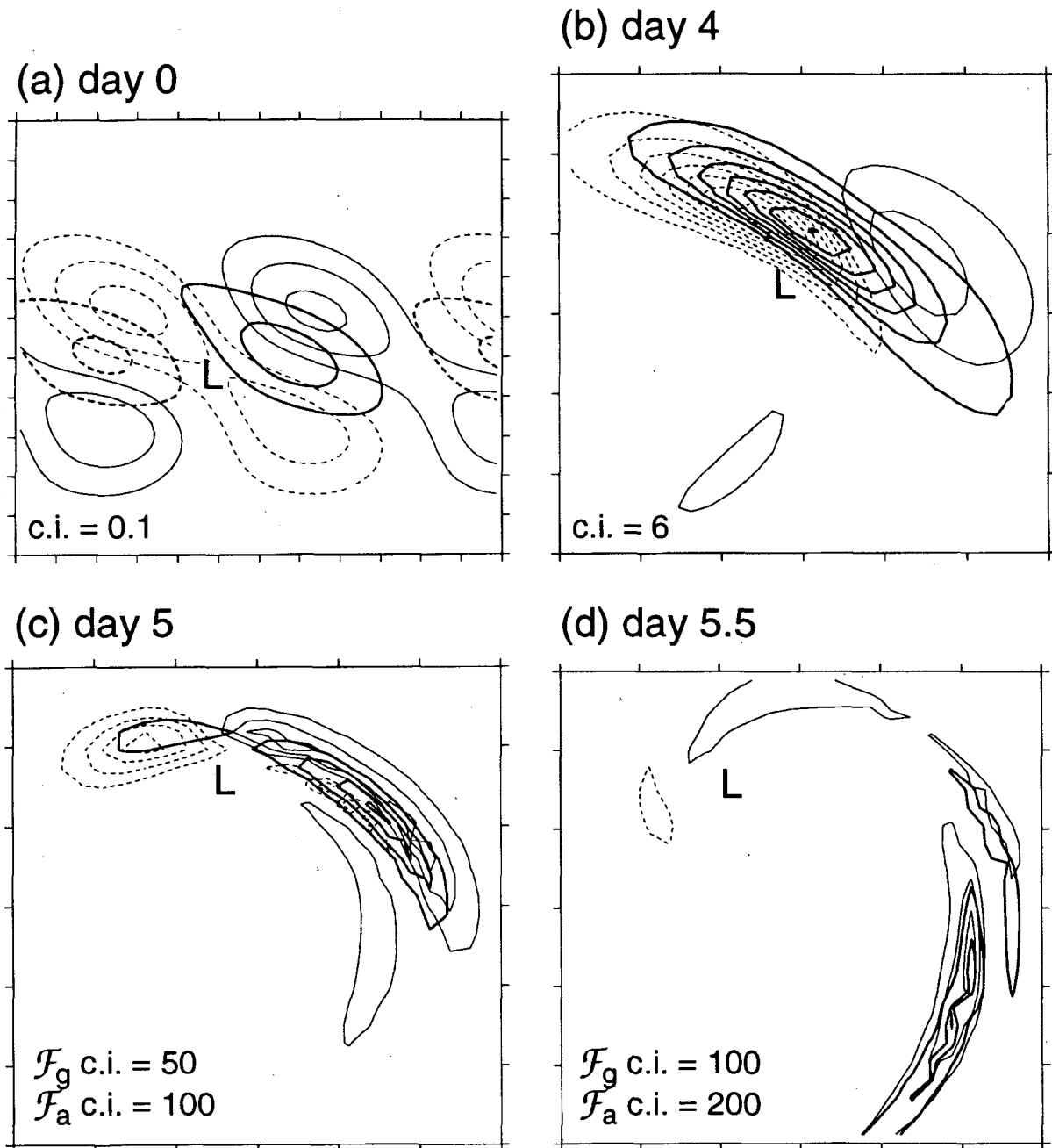
$\mathcal{F}_g$, $\mathcal{F}_a$ at the surface

FIG. 5. The geostrophic and ageostrophic frontogenesis functions $\mathcal{F}_g$ (light contours) and $\mathcal{F}_a$ (heavy contours) at the surface at (a) day 0, (b) day 4, (c) day 5, and (d) day 5.5. Contour intervals are indicated in the figures and have units of $(K/100 \text{ km})^2/10^5$ s. The plotting domains are as indicated in Fig. 3.

speed, and fluid particle motion has to be considered in an assessment of the frontogenesis.

The warm front is strongest at day 5 (Fig. 3c), but because it is so, the damping term is not negligible.

Therefore, we choose to study the warm front at day 4.5, a time before which the $|\nabla_H \theta|$ has increased to the point where the damping term becomes important. Figure 6 shows the history of the air parcel that has the
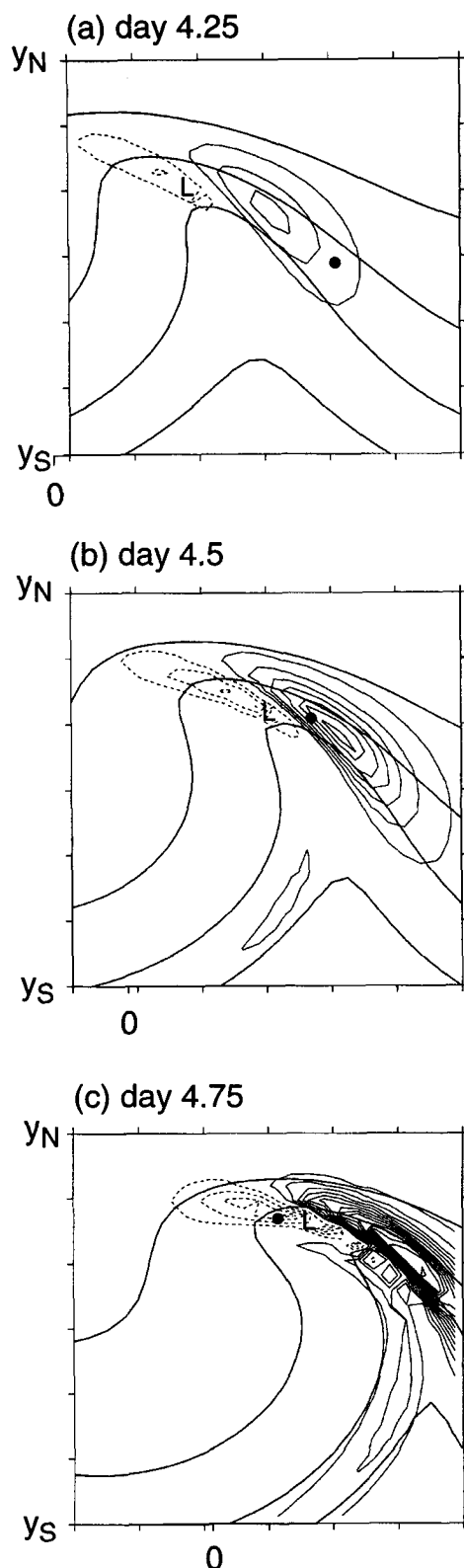
(a) day 4.25

(b) day 4.5

(c) day 4.75

Fig. 6. Plots of $\mathscr{F}$ [CI = 20 (K/100 km)^2/10^5 s], θ (CI = 10 K) at the surface at (a) day 4.25, (b) day 4.5, and (c) day 4.75. Shown is the air parcel that has the largest value of $|\nabla_H \theta|$ at day 4.5. The

TABLE 1. Analysis of frontogenesis following the air parcel shown in Fig. 6. Units of $\mathscr{F}$ are (K/100 km)^2/10^{5}s, and the $|\nabla_H \theta|$ are given in K/100 km.

Day	$\mathscr{F}_g$	$\mathscr{F}_a$	$\mathscr{F}$	$|\nabla_H \theta|_{cal}$	$|\nabla_H \theta|_{model}$
4.250	17	12	29	3.0	3.0
4.375	0	40	40	4.1	3.7
4.500	−21	145	124	5.9	5.9
4.625	−25	62	37	7.2	3.9
4.750	−130	77	−53	7.1	3.9

strongest $|\nabla_H \theta|$ at day 4.5.[6] At day 4.25 the parcel is east of the low; as it approaches the low it flows northward toward the region of strong total frontogenesis; at day 4.5 it achieves its strongest temperature gradient; by day 4.75 it flows into the zone of frontolysis. Table 1 gives a quantitative analysis of the terms in (6) for the parcel shown in Fig. 6. The ageostrophic terms are clearly the dominant contributors before and near the time when the maximum $|\nabla_H \theta|$ is achieved, while the geostrophic terms switch from weak positive to weak negative. After day 4.5, the last two columns of Table 1 show that the adiabatic calculation of $|\nabla_H \theta|$ using (6) (denoted as $|\nabla_H \theta|_{calc}$) gives values that are too large as compared with the diagnosed values of $|\nabla_H \theta|$ (denoted as $|\nabla_H \theta|_{model}$) and indicate that the effects of horizontal mixing are at work.

Just after day 5, the temperature wave breaks (Fig. 3d); the horizontal diffusion in the model allows the temperature contour to reconnect such that an isolated warm anomaly results from the breaking process and locates at the center of the cyclone. This pattern of θ and ϕ implies that $\mathbf{Q} \cdot \nabla_H \theta \to 0$ (Fig. 5d) locally. At the cold front, there is still geostrophic confluence together with ageostrophic frontogenesis acting on parcels that are slowly moving relative to the front (Fig. 7). As indicated in Fig. 5d, $\mathscr{F}_a$ reinforces $\mathscr{F}_g$ at the cold front but does not fundamentally alter the spatial distribution of the total as it does at the warm front. A quantitative analysis of the terms in (6) (not shown) simply reinforces the clear indication from Fig. 5d that both the geostrophic and ageostrophic terms are strongly positive.

[6] To compute a fluid parcel trajectory $\mathbf{x}(t)$, we integrate $d\mathbf{x}/dt = \mathbf{u}(\mathbf{x}, t)$; the solution field $\mathbf{u}$ is saved every 0.125 d, and linear interpolation in space and time is used to evaluate $\mathbf{u}$ along the parcel path.

plotting domain is 2454 km × 2454 km with y_S = 1818 km, y_N = 4272 km, which correspond, respectively, to the southern and northern edges of the window shown in Figs. 3b,c; the phase movement of the wave is marked by the $x = 0$ point.

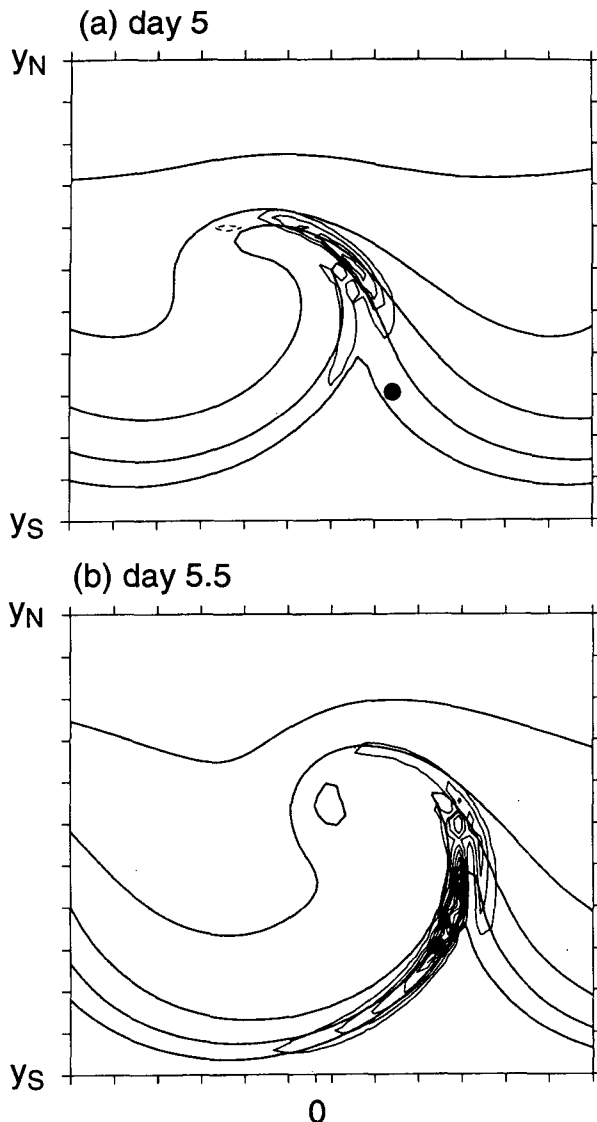## $\mathscr{F}$, θ and cold-front parcel trajectory

(a) day 5

(b) day 5.5

FIG. 7. Plots of $\mathscr{F}$ [CI = 20 (K/100 km)^2/10^5 s], θ (CI = 10 K) at the surface at the cold front at (a) day 5 and (b) day 5.5. Shown is an air parcel that has the largest value of $|\nabla_H \theta|$ at day 5.5. The plotting domain is as in Fig. 3c ($y_S = 1000$ km, $y_N = 5500$ km). Phase indicator $x = 0$ applies to both (a) and (b).

c. Analysis of the frontogenesis at the lid

Although the lid is an unrealistic constraint, the present calculations with the lid will aid in understanding the more realistic case with a tropopause.

Figure 4 contains the Q vectors at the lid. At day 0 the pattern can be understood with the approximation (10). Although the second term on the rhs is not zero at the lid, it is a secondary contributor to the total because $\partial_x\theta'$ is largest near the jet center (where $\partial_y\bar{u} \approx 0$), and $\partial_x\theta'$ is small where $\partial_y\bar{u}$ is large. Thus, the

explanation of the Q vectors in Fig. 4a is basically the same as that given for them at the surface at day 0. At the lid, however, there is a much stronger NW–SE tilt of ϕ'. Picture a line running NW–SE from north of the ridge to south of the trough; Q indicates, and Fig. 8a confirms, that there is a pattern of geostrophic frontogenesis south, and frontolysis north, of that line. By (4) there should be ageostrophic flow toward that line (recall that u_a is oppositely directed to Q at the lid); this is consistent with the ageostrophic frontogenesis shown in Fig. 8a.

This pattern intensifies and becomes a remarkably straight feature by day 4. Figure 8b shows the enhanced pattern of geostrophic frontogenesis/frontolysis that runs NW–SE from ridge to trough, and the correspondingly enhanced ageostrophic frontogenesis. At this time $\mathscr{F}_a$ is an order of magnitude greater than $\mathscr{F}_g$ and is most likely an indicator of a frontal singularity trying to form first at the lid, as predicted in HW (see their Fig. 9). At day 5 and day 5.5, the relation of $\mathscr{F}_a$ to $\mathscr{F}_g$ remains about the same upstream of the trough; at the base of the trough, however, $\mathscr{F}_a < 0$. Close examination of Q in that vicinity (Figs. 4c,d) together with Fig. 9b of Keyser et al. (1989) suggests that the latter feature is due to the nondivergent anticyclonic pattern of u_a associated with the upper low. A typical parcel that experiences upper-level frontogenesis (not shown) runs along a NW–SE corridor from ridge to trough of strong and intensifying total frontogenesis.

d. Comparison with theory and previous numerical studies

The tendency for warm frontogenesis to occur before cold frontogenesis, and the NW–SE tilt of frontal zone to the NE of the low in the developing wave, as exemplified in Fig. 3c, are common features of PE numerical simulations of baroclinic waves in meridionally limited baroclinic zones with zero or weak meridional shear at the surface [see Fig. 3 of Mudrick (1974); Fig. 4 of Newton and Trevisan (1984); Fig. 6 of Takayabu (1986); Fig. 4 of Keyser et al. (1989); Figs. 10–11 of Polavarapu and Peltier (1990)]. We believe that in all these cases the reasons for these features are as given above. For a discussion of the relevance of models of this type to observations see Shapiro and Keyser (1990, chapter 10.4).

As shown in HW, the shape of the growing mode significantly affects the placement of the frontal zones in the baroclinic wave. For reasons explored in SSR, the SG version of the shape of the growing mode is different from the PE version for the same basic state. Referring to Fig. 2 we observe that, at the surface, the SG mode is more symmetrical about the jet axis, while the PE mode exhibits a greater SE–NW tilt north of the jet axis. Our analysis (not shown) of $\mathscr{F}_g$ for the SG mode indicates that zones of warm and cold frontogenesis are more symmetrical in the SG model as com-

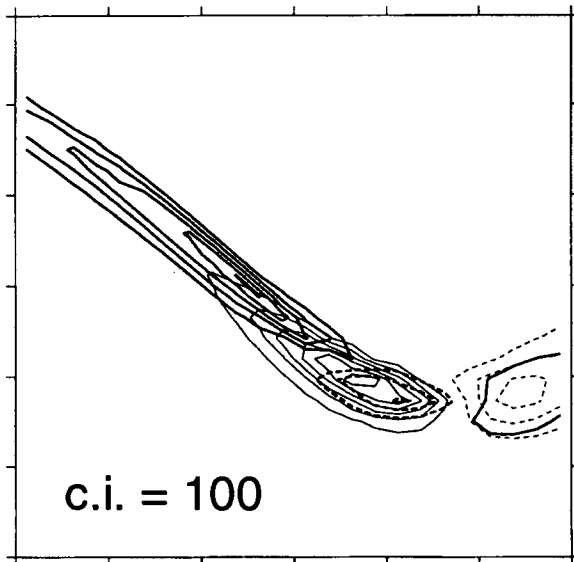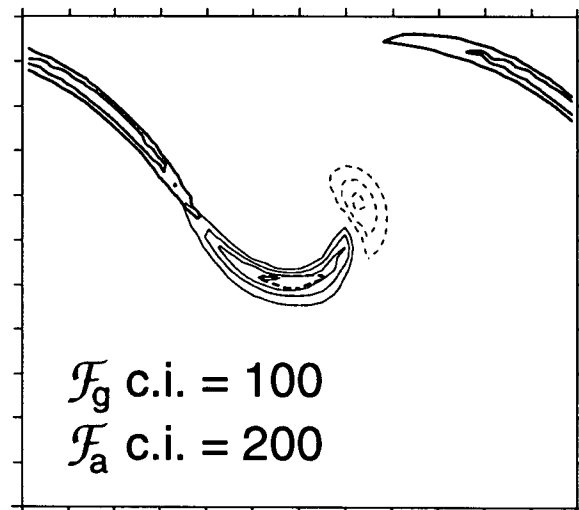## $\mathcal{F}_g$, $\mathcal{F}_a$ at the lid
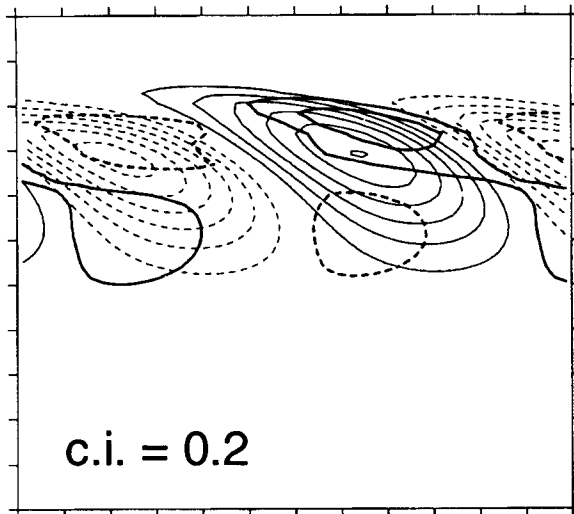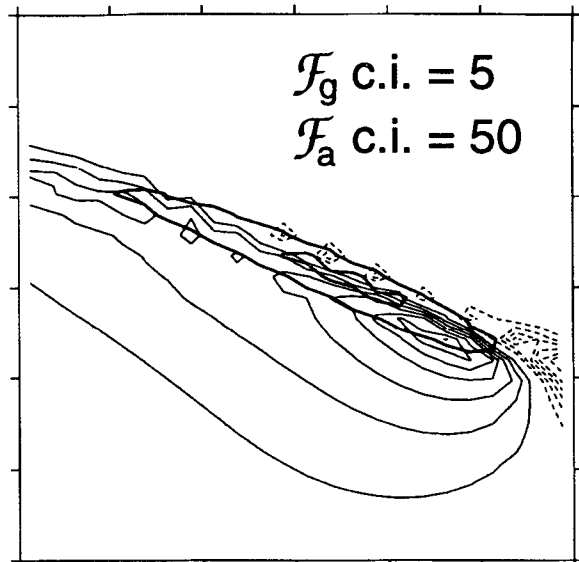
FIG. 8. As in Fig. 5 except at the lid. The plotting domains are as indicated in Fig. 4.

pared with the PE model, where the warm front is preferred (Fig. 5a). At the lid, the SG mode is nearly symmetrical about the jet axis; our analysis (not shown) of $\mathcal{F}_g$ at the lid for the SG mode indicates frontogenesis NE of the ridge and SE of the trough. The PE mode has most of its amplitude on the north side of the jet and is highly tilted NW–SE; as shown in Fig. 8a, $\mathcal{F}_g$ is highly asymmetrical with respect to

the jet indicating frontogenesis along a NW–SE line east of the ridge. Figure 4 of SSR contains a direct comparison of SG and PE showing that the fronts form as anticipated here from the modal structure.

When the baroclinic wave reaches sufficiently large amplitude, several different behaviors of the warm front among the various studies are observed. The following observations organize the available facts: a fea-
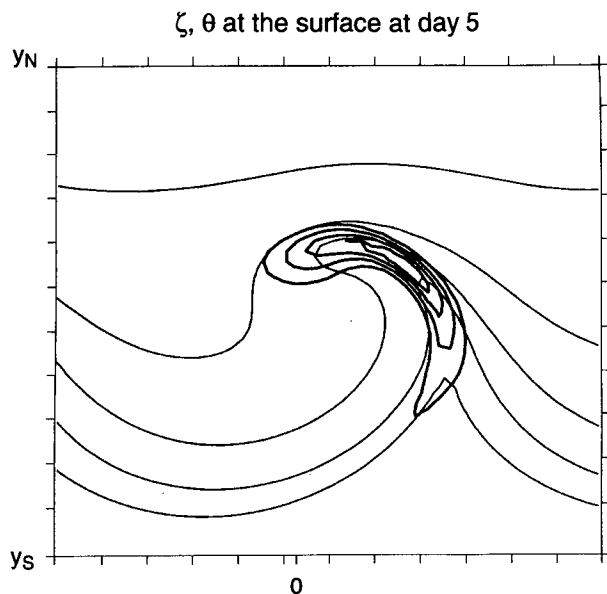
ζ, θ at the surface at day 5

FIG. 9. Relative vorticity ζ (heavy contours, CI $= 10^{-4}$ s^{-1}) and θ (light contours, CI $= 10$ K) at the surface at day 5. Plotting domain is as Fig. 3c.

sure; in contrast, the warm front is located near the center of the region of low pressure (see, e.g., Fig. 3). Hence we expect the simulated cold front to be less sensitive to the detailed shape of the high pressure region.

There is fundamental similarity of the present results with the simple HB deformation front in that a parcel experiences ageostrophic frontogenesis induced by the geostrophically induced temperature changes (Fig. 5). Figure 10 shows a vertical cross section through the front at the lid and the surface warm front at day 4 that illustrates the similarities and differences with the simple HB deformation model discussed in section 2. The view of the vertical section is to the SE, basically in the direction of the modified vertical shear. The cross section shows the temperature pattern together with w, and regions of large $|\mathscr{F}_g|$ are shaded. There are two minor departures from the simple model. First, the NW–SE zone of total warm frontogenesis at the sur-
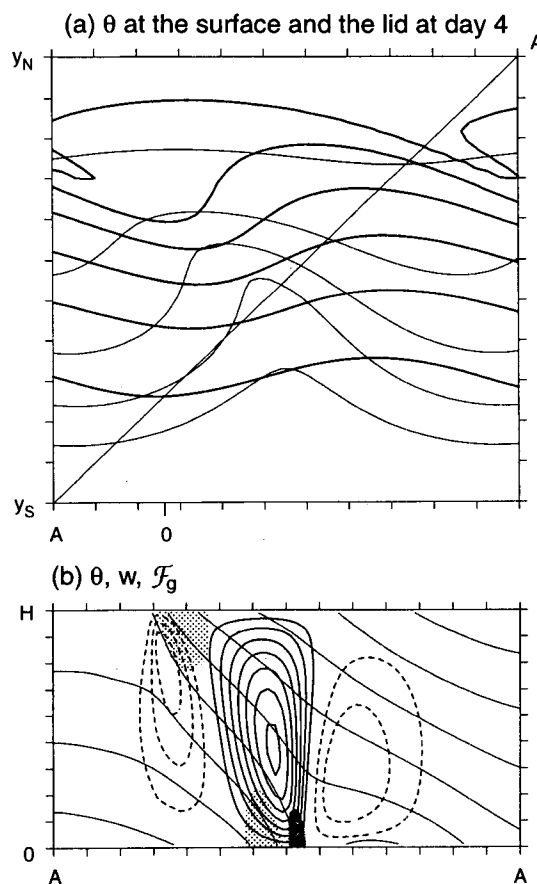
ture of all the PE simulations of baroclinic waves at large amplitude is that the warm-air sector shrinks laterally as it flows northward (evoking the image of a "tongue"), while the southward-flowing cold-air sector expands laterally. By virtue of its narrowness, the tip of the warm-air tongue is a sensitive feature; for example, Polavarapu and Peltier (1990) show a sensitivity to the inclusion of β, while Hines and Mechoso (1993) show a strong sensitivity of the warm front to surface drag. By simple invertibility reasoning (Hoskins et al. 1985), the shape of the surface low pressure pattern is linked to the shape of the tip of the warm-air tongue, and so the former is also a sensitive feature. The precise shape of the pressure field and its position relative to the temperature field (which determine the geostrophic forcing of frontogenesis) are thus sensitive features at large wave amplitude. Hence, it is difficult to make general statements about the nature of the warm front at large wave amplitude. To illustrate this, consider the recent study by Schär and Wernli (1993) where an SG model is used to compute the development from a finite-amplitude isolated disturbance in a base state with zero zonal flow at the surface. They found very little positive vorticity associated with the eastward-extending portion of the warm front in their model. In the present simulation, Fig. 9 shows there is large vorticity all along the warm front.

Cold frontogenesis is very similar among the various models, including the SG models. The SG models, like the PE models, give a shrinking warm-air sector and an expanding cold-air sector. The cold front is located at the periphery of this expanding region of high pres-

(a) θ at the surface and the lid at day 4

(b) θ, w, $\mathscr{F}_g$

FIG. 10. (a) θ at the surface (light contours) and at the lid (heavy contours); CI $= 10$ K and (b) a view of θ (CI $= 10$ K) in the vertical section cutting through both the surface warm front and the upper front with w (heavy contours, CI $= 0.5$ cm s^{-1}) superimposed; regions with light shading indicate places where $\mathscr{F}_g > 6$ (K/100 km)^2/10^5 s, while dark shading indicates places where $\mathscr{F}_g < -6$ (K/100 km)^2/10^5 s.

face has geostrophic frontolysis to the south and geostrophic frontogenesis to the north. This dipole pattern of $\mathcal{F}_g$ was noted by KSD (p. 719, see their Fig. 17b). At the lid there is also a dipole pattern, but the negative values of $\mathcal{F}_g$ are much weaker (since $|\nabla_H \theta| \approx 0$ on the north side) than the positive ones. Second, Fig. 5 shows that $\mathcal{F}_g$ evolves significantly during the time a parcel passes from ahead of the low to the place of maximum temperature gradient. These two factors, put in the context of the simple HB deformation model described in section 2, would imply that the deformation parameter α changes sign across $x = 0$ and also is a function of time.

4. Constant-potential-vorticity troposphere with constant-potential-vorticity stratosphere

a. Initial state and flow evolution

In this next case, the lid of the previous case is removed and replaced with a tropopause and stratosphere. In the appendix we give an analytic formula that closely approximates the HH base state (see their Fig. 4) and is used to generate the stronger jet used here and shown in Fig. 11. The base state is designed to have constant PV in the troposphere that is joined smoothly to another constant, but larger PV in the stratosphere. The PV increases from ~ 0.4 PVU in the troposphere to a value approximately 9 times greater in the stratosphere; PV $= 1.5$ PVU is taken as the defining value of the tropopause and is indicated by the heavy line in Fig. 11. The maximum velocity in the jet is 70 m s^{-1}, which is a little more than twice that used in HH; hence, this case is designated as HH70. For more information on the base state, see the appendix.

The reason for using a stronger jet than the one used in HH (30 m s^{-1}) is as follows. When the upper lid is replaced by a flexible tropopause, the magnitudes of the vertical velocity and vertical displacement are important factors in determining the character of the simulated upper frontogenesis, as will be discussed subsequently. Scale analysis shows that $w \sim U^2$, while vertical displacements scale as U, where U is a velocity scale for the jet. For the original 30 m s^{-1} jet used in HH, $|w|_{\max} \sim 2$ cm s^{-1} in our simulations; by increasing the speed in the base-state jet to 70 m s^{-1}, $|w|_{\max} \sim 10$ cm s^{-1}, which is closer both to observed values and to values obtained in other numerical simulations [see, e.g., Keyser and Shapiro (1986), section 4]. A 70 m s^{-1} jet is clearly a very strong flow as compared with climatology [e.g., see Bluestein (1993), chapter 2.7] but is typical of the case studies of upper-level frontogenesis reported in the literature [e.g., see Keyser and Shapiro (1986), section 2].

The domain of integration for HH70 is $y_L = 8000$ km, $x_L = 4000$ km, and $H = 15$ km. The x, y, and z directions are covered respectively by 40, 80, and 60 grid intervals so that $(\Delta x, \Delta y, \Delta z) = (100, 100, 0.25$ km).

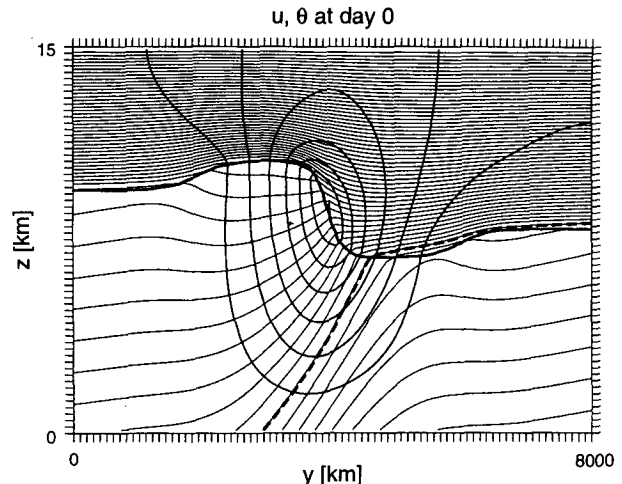u, θ at day 0

FIG. 11. Zonal velocity (heavy contours, CI $= 10$ m s^{-1}) and potential temperature (lighter contours, CI $= 5$ K) for the HH70 jet (constant-PV troposphere beneath a constant-PV stratosphere). For this study, the maximum velocity in the jet is 70 m s^{-1} (in HH, a 30 m s^{-1} jet was used). The thick solid line denotes the PV $= 1.5$ PVU line, which represents the tropopause. The $\theta = 305$ K line is dashed, as it will be referred to subsequently. Grid intervals are indicated by the tick marks.

As in the previous case, the most unstable normal mode is computed and found to have a doubling time of ~ 1 d, somewhat slower than HW60; slower growth with a flexible tropopause is expected based on theory (Rivest et al. 1992), presumably due to the effectively weaker meridional PV gradient at the flexible tropopause. The phase speed of the mode is 23 m s^{-1}. The general shape of the mode in the troposphere is similar to that of the HW60 mode (Fig. 2); so is, moreover, the time evolution (starting from the normal mode as described in section 2) until about day 6. Also, the evolution of the surface flow is substantially the same as in HW60 throughout the integration period (9 days). Therefore, we concentrate here on the upper frontogenesis, which is substantially different.

Upper-level frontogenesis is, by historical precedent, taken to be the increase of $|\nabla_H \theta|$ over time. As with frontogenesis at the surface, it occurs within a certain sector of the evolving baroclinic wave. What makes the upper-level frontogenesis more complex than the surface frontogenesis is that the vertical motion is not restrained to be zero on the horizontal surface in question. To gain an appreciation of the fully three-dimensional nature of the flow in which the front forms, we show its evolution from two different perspectives—first from the constant-height view, then from a three-dimensional view.

Figure 12 displays the wave-relative horizontal velocity vectors, the vertical velocity, and the PV in intervals of 1.5 PVU, starting with the 1.5 PVU value at $z = 6$ km for $x \in (0, 4800)$ km (the $x = 0$ location is chosen arbitrarily relative to the wave) and $y \in (2000,$

u$_{rel}$, w, PV at z = 6 km
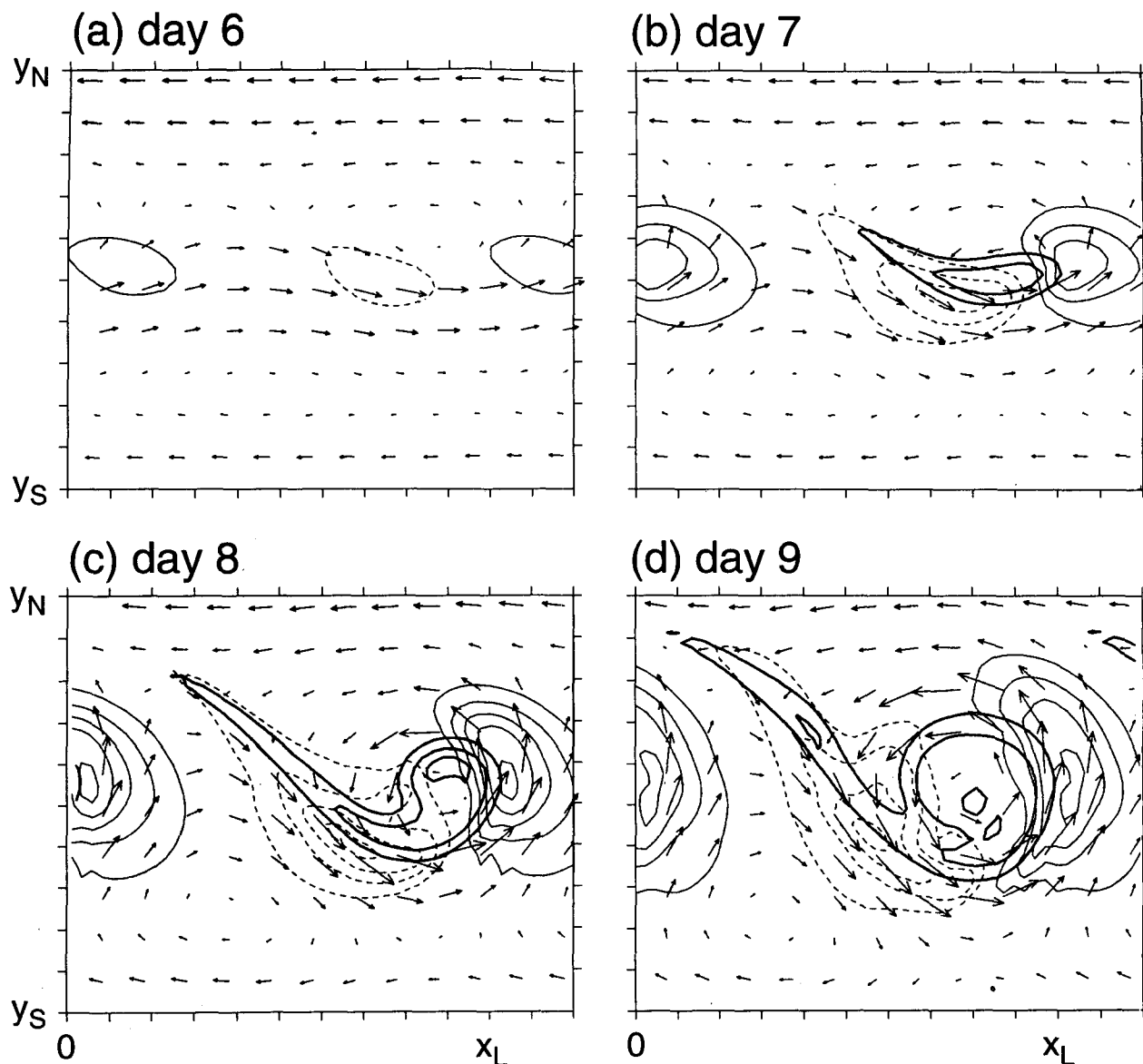
(a) day 6

(b) day 7

(c) day 8

(d) day 9

FIG. 12. Wave-relative horizontal velocity vectors u_{rel}, vertical velocity (light contours, CI = 2 cm s^{-1}), and PV (heavy contours, CI = 1.5 PVU, starting with the 1.5-PVU line) at z = 6 km for $x \in$ (0, 4800) km (wave relative) and $y \in$ (2000, 6000) km for (a) day 6, (b) day 7, (c) day 8, and (d) day 9. The distance between tick marks is 4Δx (400 km); a velocity vector of this length indicates a wind speed of approximately 40 m s^{-1}. Vectors plotted every 4Δx.

6000) km. At day 6 (Fig. 12a) the flow pattern is basically that of the linear mode with rising (sinking) motion east (west) of the upper cyclone; high-PV air is still above the z = 6 km level. As the pattern amplifies, Fig. 12b shows that by day 7 high-PV air has descended through the z = 6 km level near where $w < 0$ and the wave-relative horizontal motion is slow. By day 8 (Fig. 12c), the fish-shaped zone of high-PV air expands—the tail extends farther westward toward the

ridge, and the head curves cyclonically into the center of the generally more intense cyclone. Low-PV air enters into the same locale after having risen and entered from around the east side. Thus, we observe a three-dimensional stirring of the high- and low-PV airstreams. There is evidence of diffusively created PV (cf. Cooper et al. 1992) in Fig. 12, since the highest value in the initial state is only 3.6 PVU. By day 9 (Fig. 12d), the high-PV air is now at the center (and three-

dimensional stagnation point) of an eddy with three-dimensional flow structure, essentially an upper-level "cutoff" cyclone.

Figure 13 displays θ, ϕ, and $\mathbf{Q}$ in the same way as done for HW60 (Fig. 4). At day 6 (Fig. 13a), θ and ϕ are substantially in phase near the jet center, just as in HW60 (Fig. 4), and just as the simple argument of HW (p. 1679) predicts. At day 7 (Fig. 13b) there is a strong departure from this pattern as the isotherms begin to cross the lines of constant ϕ just upstream of the trough. Looking back to Fig. 12b, it is clear that this development is associated with the descent of high-PV air through the $z = 6$ km level. This feature intensifies further by day 8 (Fig. 13c). By day 9 (Fig. 13d), the isotherms within the cutoff are nearly perpendicular to the NW–SE orientation of the frontal zone.

Vertical cross sections through the flow at day 9 (Fig. 14; sections indicated in Fig. 13d) show the fine-scale of the downward PV extrusions (to less than 3 km in Fig. 14b) associated with the frontal features.

θ, ϕ, $\mathbf{Q}$ at z = 6 km
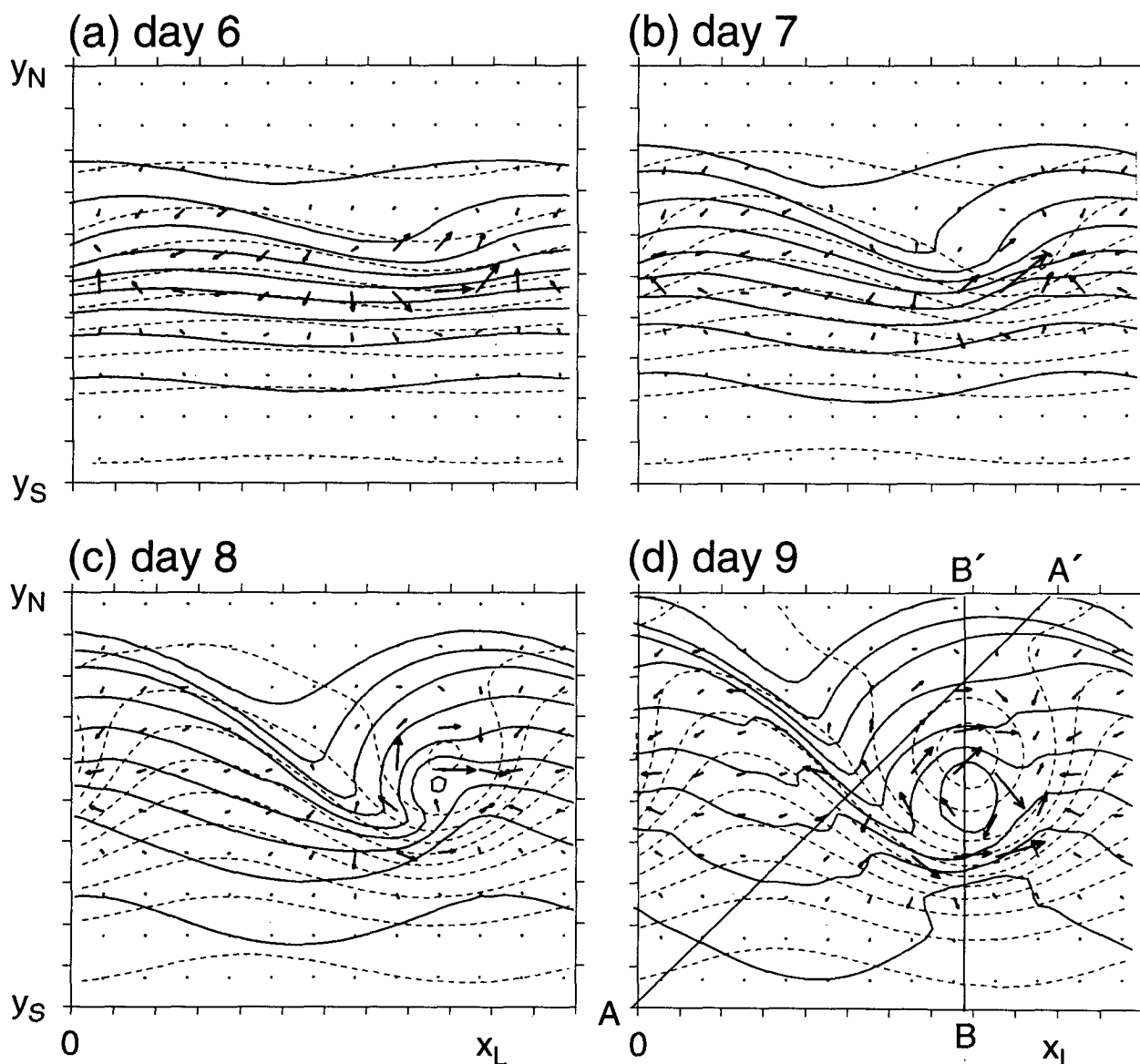

FIG. 13. Evolution of θ (solid lines, CI = 5 K), ϕ (dashed lines, CI = 1000 m^2 s^{-2}), and $\mathbf{Q}$ (vectors plotted every $4\Delta x$; units not relevant) at $z = 6$ km on same domain as in Fig. 12 for (a) day 6, (b) day 7, (c) day 8, and (d) day 9.
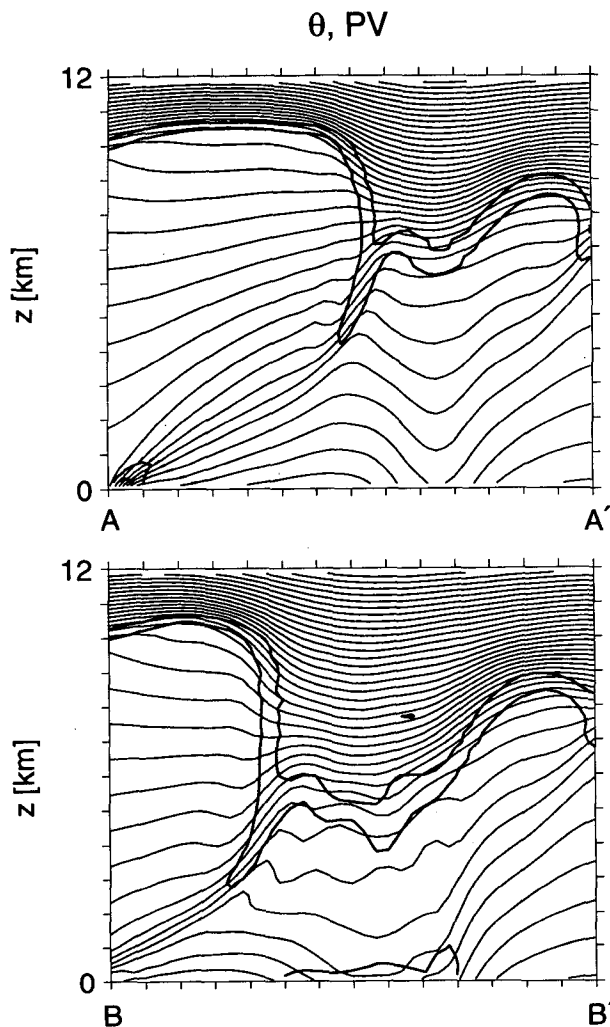
θ, PV

FIG. 14. Vertical cross sections at day 9 showing θ (CI = 5 K) and PV (two heavy solid lines marking the 1.5- and 3.0-PVU surfaces) for a NE–SW section through the northwesterly flow (upper panel), and a N–S section through the trough, shown in Fig. 13d.

Also, these two cross sections give an impression of the strong three-dimensional variation of the tropopause at this stage.

The fronts develop when the baroclinic wave is rapidly evolving through the large amplitude stage to the stage of wave breaking. Even leaving aside the dynamics, a bare kinematical description of the flow is difficult. Figure 13 suggests that, at the very center of the cyclone, the isentropes have a rather complex structure. To illustrate this, consider the θ field at $z = 4$ km in Fig. 15; the 305-K contour is marked by the heavy line. The 305-K line develops a complex structure by day 8. In Fig. 16 we follow fluid particle trajectories backward in time from the locations indicated in Fig. 15c. Trajectories labeled A, B show air descending from the west, while trajectory E shows air ascending from the east of the cyclone [cf. Fig. 1 of Thorncroft et al.

(1993) and references]. Trajectory C shows that the warm anomaly is associated with flow rising up on the east side of the cyclone from below to above the $z = 4$ km level but then descending to its location at day 8. Trajectory D shows that the cold anomaly is associated with flow descending form the northwest below, then rising again to, the $z = 4$ km level at day 8. Figure 17 shows a three-dimensional image of the 305-K isentrope from a perspective looking down from the SE. The severe contortions of the 305-K surface illustrate the mixing process indicated by trajectories C and D in the previous figure. The three-dimensional ridge containing lower-θ air protrudes toward the SE and wraps cyclonically around a higher-θ valley, which builds and wraps cyclonically with the ridge. At day 8 one can now visualize how trajectory C represents air from the valley, and trajectory D represents air from the ridge.

To understand the flow as the wave breaking (cutoff formation) process occurs, it has been suggested (Hoskins et al. 1985, section 8) that viewing the PV as it moves along θ surfaces is preferable to the traditional constant pressure (or height, in the present context) view. Regions of high-PV air (PV > 1.5 PVU) are "painted" onto the 305-K surface shown in Fig. 17. As discussed by Hoskins et al. (1985) high-PV air rides down the isentrope from the stratosphere, while low-PV air rides up from the troposphere; the low- and high-PV streams begin to wrap cyclonically around each other from day 6 to day 7. By day 8, however, there is strong creation of PV in the surface fronts (cf. Cooper et al. 1992) and strong distortions at higher levels due to mixing. The final equilibrium state of the PV is not easy to predict since PV does not obey a simple downgradient mixing law (see Keyser and Rotunno 1990 and references).

Another view of the development is shown in Fig. 18 by means of a three-dimensional image of the 1.5-PVU surface on $x \in (800, 4800)$ km, $y \in (2000, 6000)$ km, and $z \in (6, 12)$ km; the view is from the ground looking upward and westward. As time passes, there is a large downward excursion of a "tongue" of high-PV air; the slice through the $z = 6$ km level shows how the constant-height PV contours of Fig. 12 relate to the three-dimensional field.

b. Analysis of the upper-level frontogenesis

Near day 7 (Fig. 13b), the map of θ and ϕ is basically the same as in previously published studies of upper-level frontogenesis using PE models [cf. Fig. 7 of Shapiro (1975); Fig. 2 of Buzzi et al. (1977); Fig. 10a of Newton and Trevisan (1984); Fig. 4 of Keyser et al. (1989)]. In these studies, the front is identified with the strong horizontal temperature gradient near where $\nabla_H \theta$ turns sharply from southward to eastward pointing. In the present case, another zone of strong $|\nabla_H \theta|$ running NW to SE from the ridge toward the trough develops by day 8 and also becomes a promi-
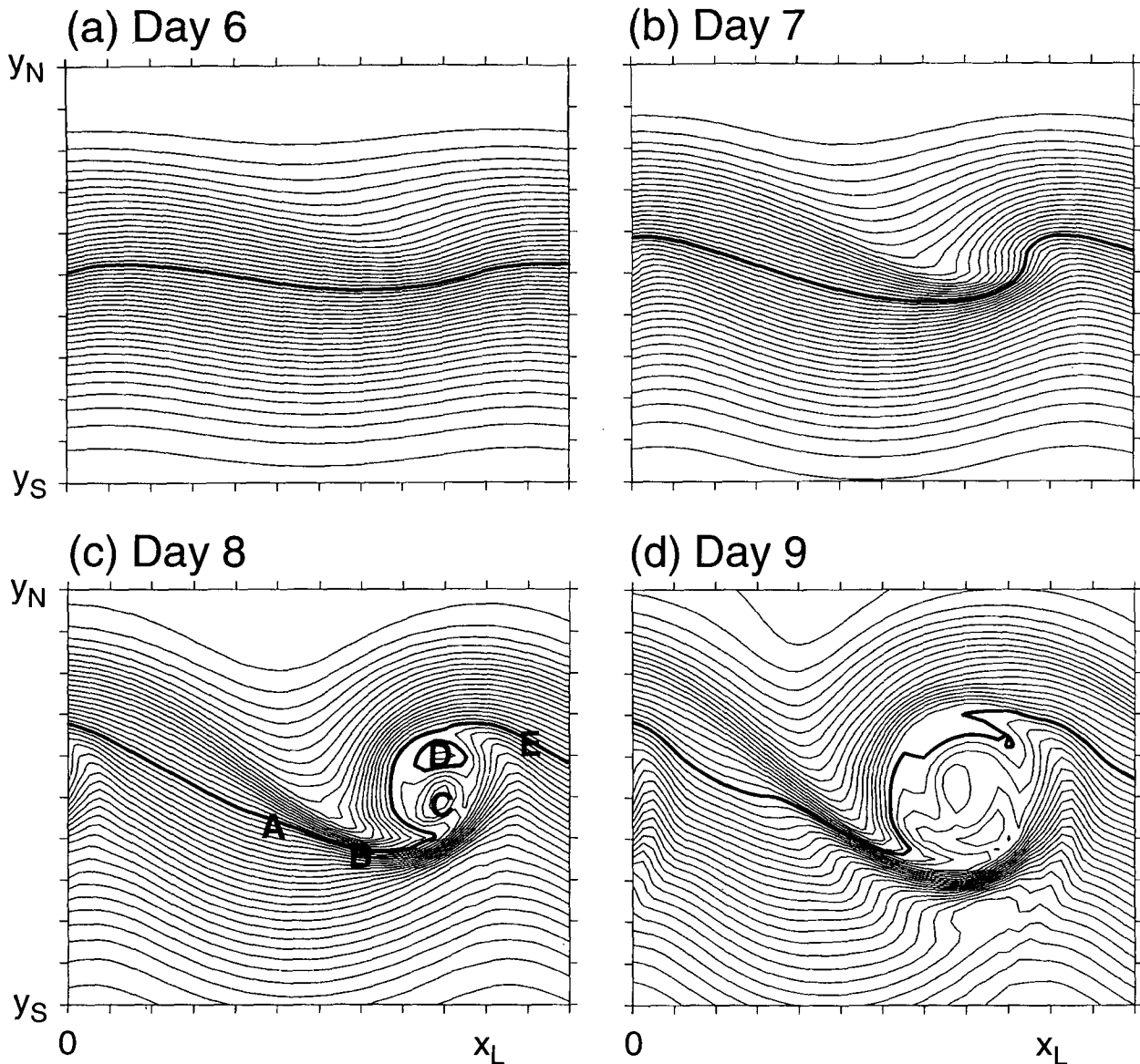
θ at z = 4 km

(a) Day 6

(b) Day 7

(c) Day 8

(d) Day 9

FIG. 15. Evolution of θ (solid lines, CI = 1 K; heavy line is the 305-K contour) at z = 4 km on same domain as in Fig. 12 for (a) day 6, (b) day 7, (c) day 8, and (d) day 9. Air parcels for the trajectory analysis shown in Fig. 16 are indicated by the letters in (c).

nent feature [cf. Fig. 13d with Fig. 7 of Hines and Mechoso (1991)].

Figure 13a shows that at day 6 the pattern of **Q** is basically the same as in Fig. 4a with divergence of **Q** along a line running NW to SE between the ridge and the trough. The reasons for the pattern are also the same: due to the NW–SE tilt of the mode, there is geostrophic confluence to the SW, and geostrophic difluence to the NE, of the NW–SE line. The implied horizontal ageostrophic motion (4) is in the opposite direction to **Q** and so enhances frontogenesis along that NW–SE line as in the case with the lid (Fig. 8a).

At day 7 (Fig. 13b) there is dramatic change in the pattern of θ and ϕ as mentioned above. Previous to this development, the large-scale wave grows with θ and ϕ mostly in phase. After this development, there is a local change in the pattern of θ and ϕ such that there is strong cold advection just SW of the trough. This development implies a significant change in the **Q**-vector distribution: The pattern of θ and ϕ implies a frontolytical geo-
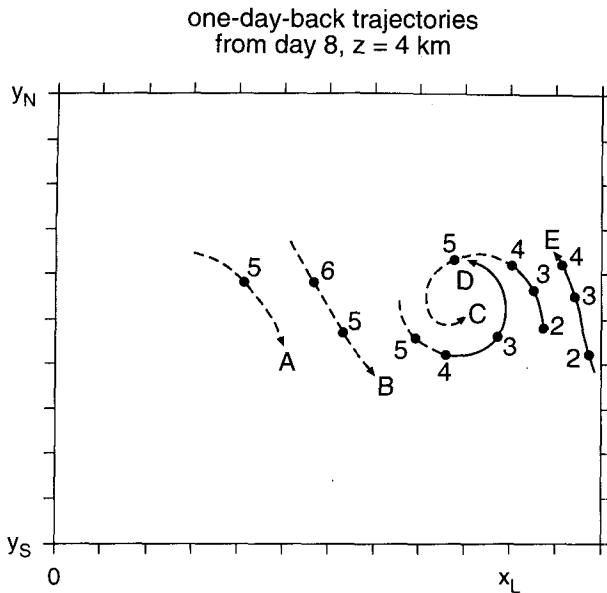
one-day-back trajectories
from day 8, z = 4 km

FIG. 16. Day-long wave-relative fluid parcel trajectories ending at the $z = 4$ km level at day 8 as indicated in Fig. 15c. Large dots indicate places where a parcel attains the height (in km) indicated by the adjacent number; dashed (solid) lines indicate a parcel height above (below) 4 km. The mixing process between the warm air rising from the SE and the cold air sinking from the NW is illustrated by trajectories C and D.

strophic horizontal shear that makes **Q** point toward cold air on the cyclonic shear side of the jet; with **Q** continuing to point toward warm air on the anticyclonic shear side of the jet, a strong divergence of **Q** occurs along the jet [see Shapiro (1981) and Keyser and Pecnick (1985); we refer to this below as the "Shapiro effect"]. This is the feature analyzed as the upper front by KSD and others. The pattern intensifies at day 8 (Fig. 13c) but is more difficult to identify at day 9 (Fig. 13d).

An analysis of the frontogenetical functions at day 7 is given in Fig. 19. In consequence of the Shapiro effect, the dominant feature in the $\mathscr{F}_g$ field is the strong dipole pattern. Although it is relatively weak at this time and does not appear on the contour plot, there is also a signature of $\mathscr{F}_g > 0$ in the NW–SE corridor running from ridge to trough, just upstream of the dipole pattern. The total frontogenetical forcing due to the horizontal wind component $\mathscr{F}_g + \mathscr{F}_a$ is nearly the same as $\mathscr{F}_g$, showing that $|\mathscr{F}_a|$ is small at this time. The most important contribution to frontogenesis at this time is accomplished through differential vertical motion as indicated by $\mathscr{F}_{tilt}$ in Fig. 19c. The total frontogenetical function $\mathscr{F}$ is shown in Fig. 19d; $\mathscr{F}_{tilt}$ is obviously the main contributor.

The same analysis is shown for day 9 in Fig. 20. Here one can clearly identify two types of frontal zone in the analysis, even though the front at day 9 (Fig. 13d) appears as a single, more or less continuous fea-

ture. The field of $\mathscr{F}_g$ shows two distinct zones: one NE of the ridge and the other SW of the trough. The latter is the remnant of the dipole pattern shown at day 7 (Fig. 19). The pattern of $\mathscr{F}_g + \mathscr{F}_a$ shows that $\mathscr{F}_a < 0$ SW of the trough as it did in the case with a lid at the late stage (Figs. 8c,d). Tilting continues to be the dominant effect along this front (Fig. 20c). Along the front NE of the ridge, the pattern of $\mathscr{F}_g + \mathscr{F}_a$ shows that $\mathscr{F}_a > 0$ and $\mathscr{F}_{tilt} < 0$. Along this part of the upper front there is similarity to the case with the lid (cf. Fig. 8b) in that $\mathscr{F}$ is composed mainly of $\mathscr{F}_g + \mathscr{F}_a$.

To give a more complete picture of the upper frontogenesis, we return to a trajectory analysis at day 8. In Fig. 21 the trajectory labeled A is that of an air parcel that is part of the front NE of the ridge; the one labeled B is for the one just SW of the trough. Table 2 contains the Lagrangian history of the frontogenetical forcing for the half-day preceding the final positions shown in Fig. 21. The table shows that the frontogenesis on trajectory B reflects the Shapiro effect since there is negative geostrophic forcing, and the frontogenesis is due to tilting. For trajectory A, the frontogenesis is due mainly to the horizontal motion, as in the case with a lid.

Figure 21 contains the trajectory labeled C of an air parcel that is part of the front at $z = 4$ km. At this lower level, the wrapping of the θ contours is at a more advanced stage than at the $z = 6$ km level. Hence, the Lagrangian history reflects the balances indicated in Fig. 20 for day 9 at $z = 6$ km; Table 2 shows that tilting is the dominant contributor, as geostrophic and horizontal ageostrophic effects tend to offset each other.

The preceding analysis suggests to us the following way of thinking about upper frontogenesis. Starting with the broad and proceeding toward the particular, we first notice that the nature of the frontogenetical forcing changes remarkably in going from the pre-wave breaking to the post–wave breaking stage.

In the pre–wave breaking stage, which is the stage considered by almost all past investigators, the chain of cause and effect runs like this: Consider in the first step the flow in Fig. 13a—the isolines of θ and ϕ are roughly parallel but there is small amount of geostrophic confluence south, and difluence north, of a NW–SE line running from ridge to trough. The ageostrophic response indicated by **Q** is horizontal motion toward that line and sinking motion along it. This implies frontogenetical tilting to the north and frontolytical tilting to the south of that line. As the sinking motion grows in intensity with distance from the ridge along the line, and in time, higher-θ air from aloft descends past the $z = 6$ km level; this implies that the isotherms on this level will no longer be roughly parallel to the lines of constant ϕ but rather will turn sharply near the trough as shown in Fig. 13b. With this new pattern of θ and ϕ, there is a strong local divergence of **Q**, since now there is a combination of cold advection and confluence implied by that pattern (Sha-
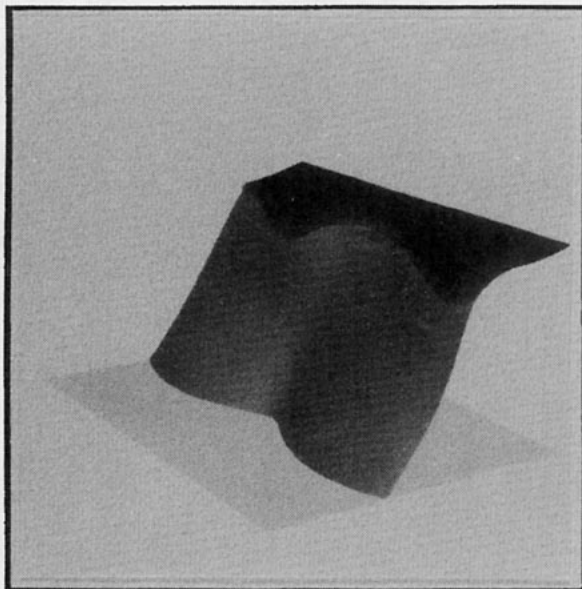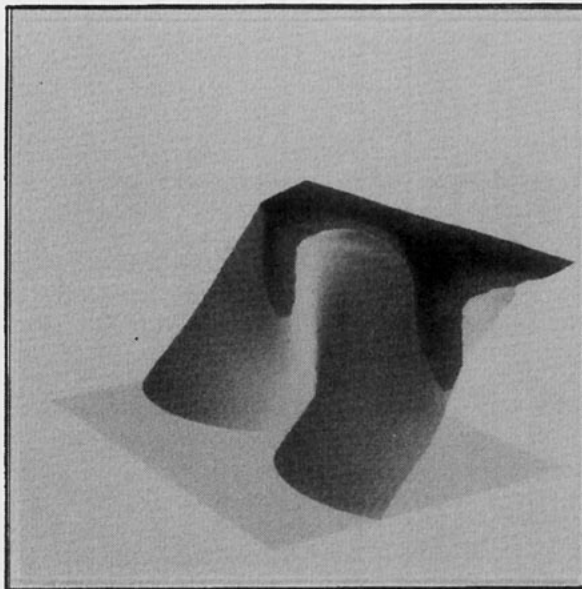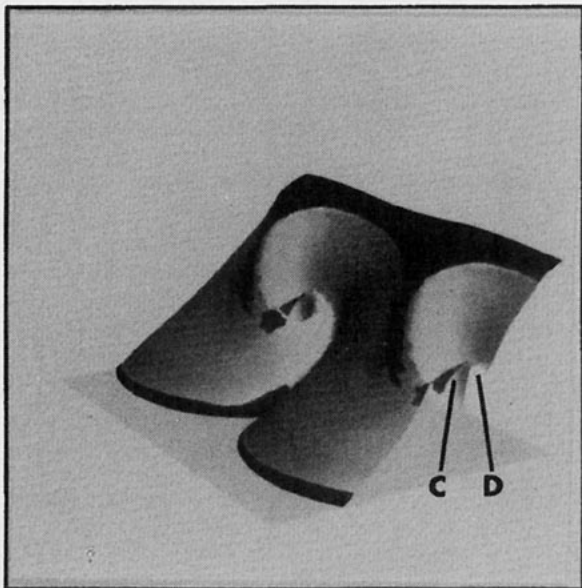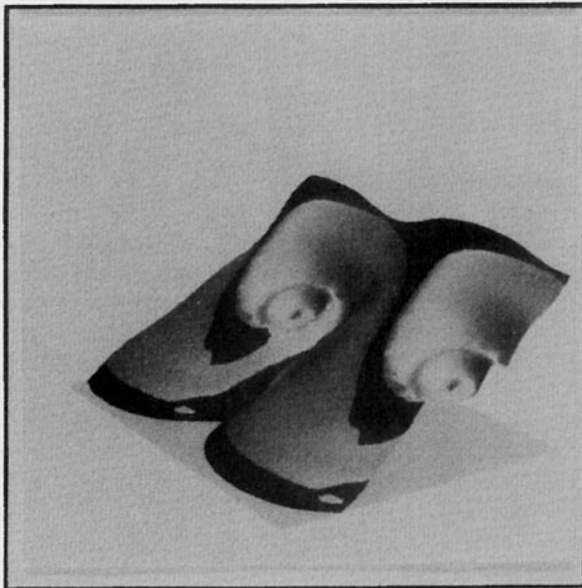
FIG. 17. Three-dimensional view of the 305-K isentropic surface at (a) day 6, (b) day 7, (c) day 8, and (d) day 9. Regions of PV > 1.5 PVU are "painted" on the surface. Approximately one and three-quarters of a wavelength is displayed to give a vertical cross-sectional view at the eastern end of domain. Positions of parcels C and D (Fig. 15c) are indicated in (c).

piro 1981; Keyser and Pecnick 1985). This divergence of Q implies stronger vertical motions that will then produce stronger tilting; hence, one can understand the local intensification of the front in the vicinity of the trough.

What we find of further interest is the implication of the Shapiro effect for the continued development of the flow pattern. For if the effect of the sinking motion is to turn the isotherms away from the lines of constant ϕ, and if this in turn generates stronger sinking motion, there is then implied a further cyclonic turning of $\nabla_H \theta$ away from $\nabla_H \phi$, consistent with the pattern shown in Fig. 13c. Note that at day 7 (Fig. 13b) there is a rough symmetry of the Q pattern with respect to the trough
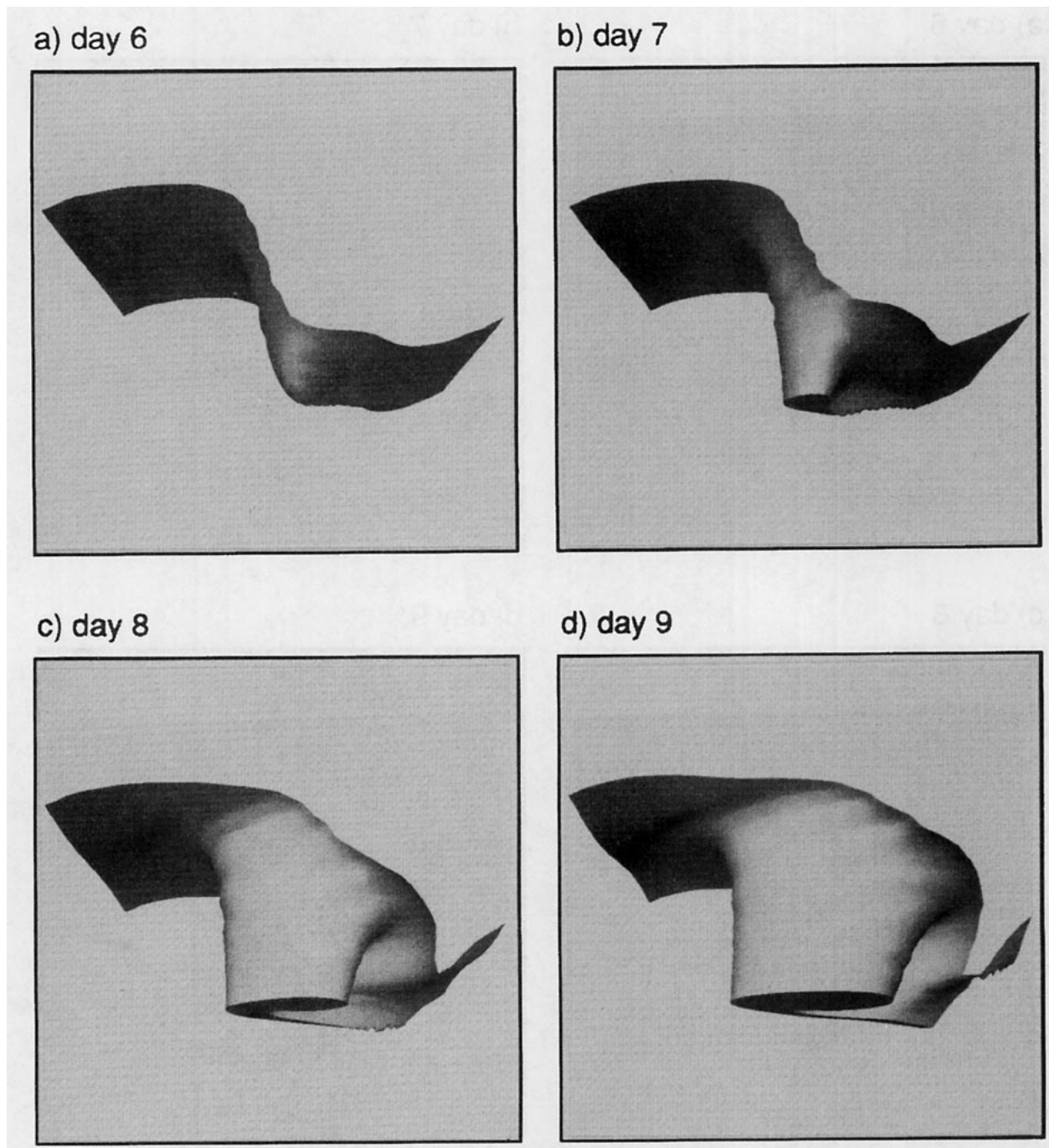
FIG. 18. Three-dimensional view (from the surface looking upward and westward) of the 1.5-PVU surface at (a) day 6, (b) day 7, (c) day 8, and (d) day 9. In this plot, the horizontal display domain is $x \in (800, 4800)$ km and $y \in (2000, 6000)$ km; in the vertical $z \in (6, 12)$ km. As the high-PV air descends below $z = 6$ km, the shape of the PV = 1.5 PVU line in Fig. 12 is seen.

since downstream there is convergence of $\mathbf{Q}$ and rising motion. However, by day 8 (Figs. 12c, 13c) this symmetry is disrupted as air from various levels has started to collect within the nascent eddy (region of closed wave-relative streamlines). The formation of the eddy arranges the isentropes within the eddy so that they are nearly perpendicular to the frontal zone. Although $\mathbf{Q}$ still

points toward cold air, the weakening of the temperature gradients within the eddy means that the negative part of the dipole pattern of $\mathscr{F}_g$, the signature of the Shapiro effect, disappears (cf. Fig. 20a with Fig. 19a). Moreover, the ageostrophic circulation due to $\mathbf{Q}$ within the eddy is in the alongfront direction and hence not able to participate in a feedback. Thus, in the post–wave break-

θ and frontogenetical functions
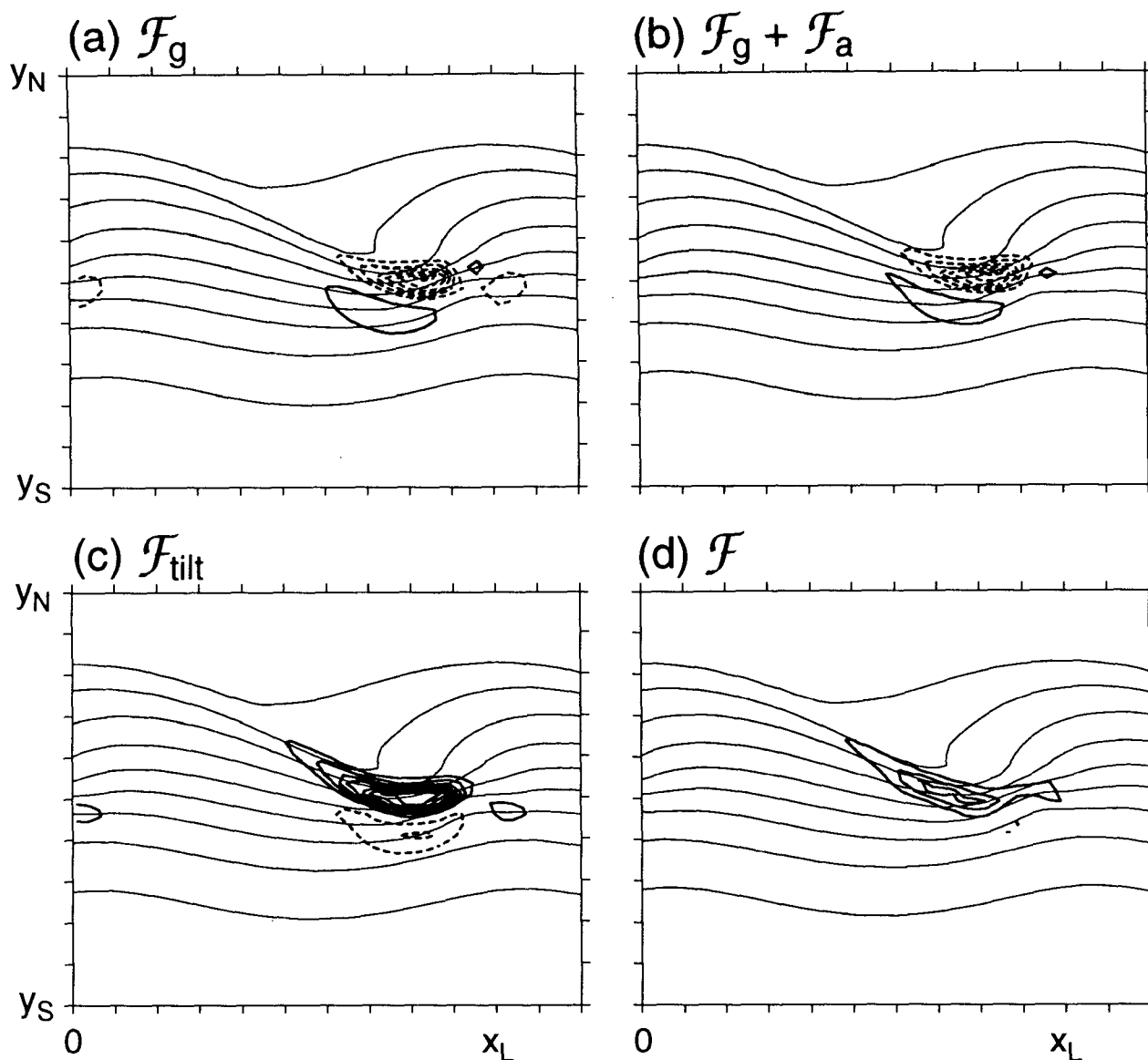# at z = 6 km, day 7

(a) $\mathcal{F}_g$

(b) $\mathcal{F}_g + \mathcal{F}_a$

(c) $\mathcal{F}_{tilt}$

(d) $\mathcal{F}$

FIG. 19. Plot of θ (light solid lines, CI = 5 K) at day 7 at z = 6 km on the same domain as shown in Figs. 12c and 13c displayed with (a) $\mathcal{F}_g$, (b) $\mathcal{F}_g + \mathcal{F}_a$, (c) $\mathcal{F}_{tilt}$, and (d) $\mathcal{F}$. For all $\mathcal{F}$ CI = 20 (K/100 km)^2/10^5 s.

ing stage, the upper frontogenesis in the vicinity of the trough is still produced by tilting, but the vertical motion is due mainly to the divergence of a Q pattern wherein all the Q vectors point toward higher θ.

c. Comparison with theory and previous numerical studies

In the following we rely heavily upon the comprehensive review of upper-level frontogenesis conducted by Keyser and Shapiro (1986). The universal conclusion from observation and numerical studies is that the proximate cause of intense upper-level frontogenesis is tilting [Eq. (9)]. Most (but not all) observed cases show that the upper front forms in the northwesterly flow between the ridge and the trough in an amplifying baroclinic wave [the recent study by Sanders et al. (1991) is particularly relevant]. In numerical simulations on the sphere, Hines and Mechoso (1991) showed

θ and frontogenetical functions
at z = 6 km, day 9

(a) $\mathcal{F}_g$

(b) $\mathcal{F}_g + \mathcal{F}_a$
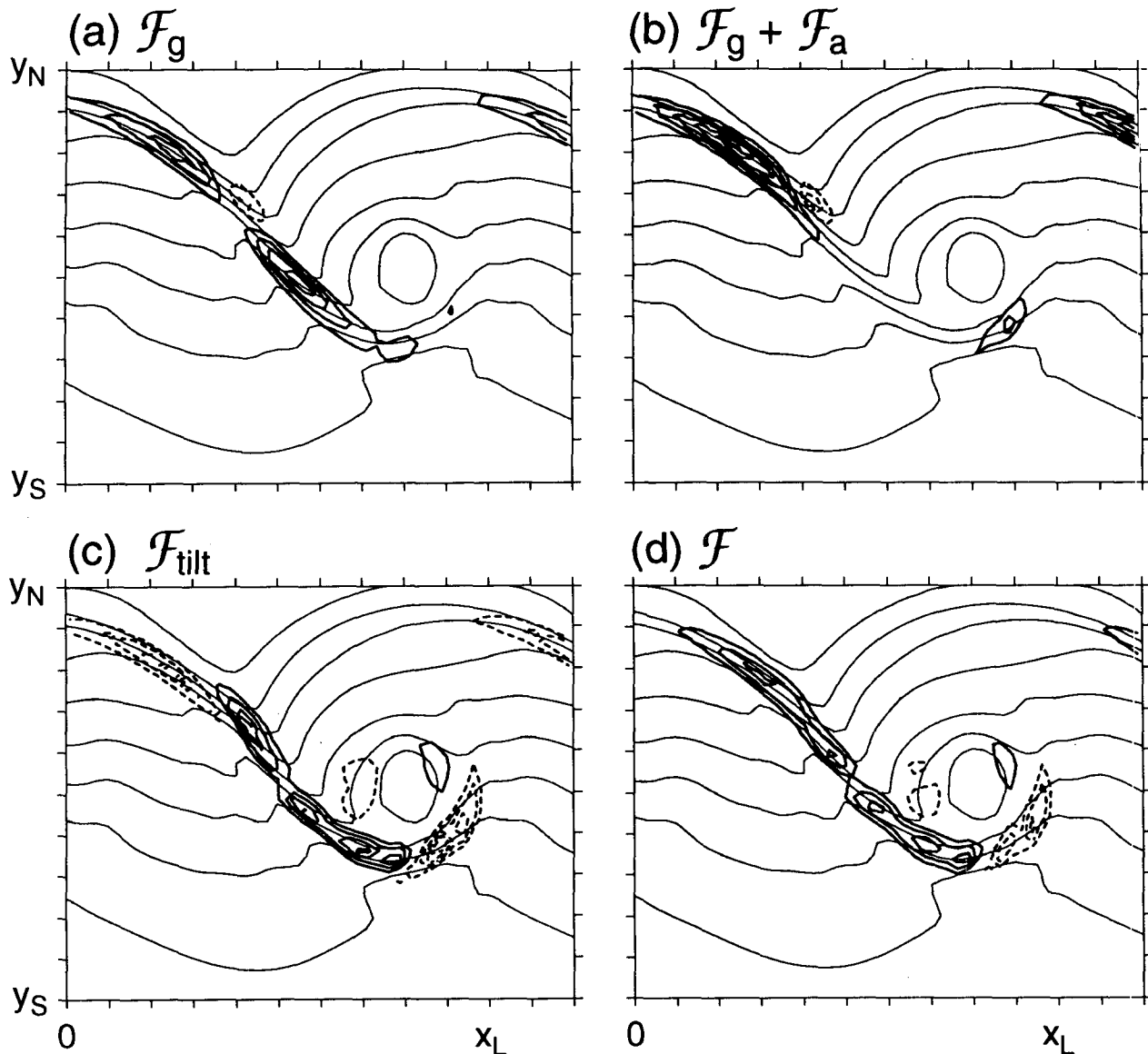
(c) $\mathcal{F}_{tilt}$

(d) $\mathcal{F}$

FIG. 20. As in Fig. 19 but for day 9.

that for a certain base state, the position of the upper front develops downstream of the upper trough (see section 3d).

With regard to the SG simulations of upper frontogenesis by HH, the same remarks apply as were made about the upper frontogenesis in the SG simulations of frontogenesis at the lid in HW (see section 3d). As mentioned in section 1, the SG study by HH used a jet with a maximum speed of 30 m s^{-1}. Integrations with the PE model using this flow gave relatively weak ver-

tical motion throughout the integration (peak magnitudes ~2 cm s^{-1}). An analysis of the upper-level frontogenesis in that simulation, similar to that given in Figs. 19 and 20 and Table 2, showed a negligible role for tilting and, in fact, indicated a frontogenesis scenario similar to the case with a lid. The character of the frontogenesis changes with the jet speed because the magnitude of the vertical displacements produced by the growing wave depends on the jet speed. The vertical displacements scale as U and are apparently too
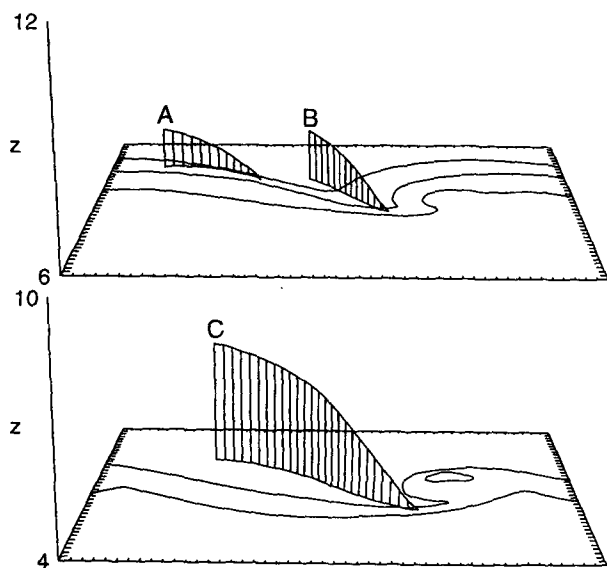
FIG. 21. Three-dimensional one-day-back trajectories of parcels having the largest $|\nabla_H \theta|$ from $z = 6$ km (upper panel) and $z = 4$ km. The θ contours at $z = 6$ km are those flanking the zones of strong $|\nabla_H \theta|$ (cf. Fig. 13c); similarly for the two contours shown at $z = 4$ km (cf. Fig. 15c); in both cases, the contour interval is 10 K. Horizontal domain is as in Fig. 13c; grid intervals are indicated by the tick marks.

small to activate the tilting process when the jet speed is 30 m s^{-1}.

Following the wave development from the small amplitude stage allows one to develop a definite sequence of cause and effect. In many studies the first analysis time corresponds to about day 7 in the present study; the phase lag between the geopotential wave and potential isotherm wave is taken as the natural signature of the developing baroclinic wave (Keyser and Shapiro 1986). However, as shown by HW for the case with a lid and evinced by the numerical calculations with a tropopause shown here, phase lag is very small until the wave grows to finite amplitude. It is a consequence of the intensifying field of vertical motion that the θ field is so modified that isolines of ϕ and θ come to cross on a level surface. Once this occurs, a strong divergence of Q is implied, for the reasons described by Shapiro (1981) and Keyser and Pecnick (1985). The latter then implies intensified vertical motion and stronger tilting. Since all of the baroclinic wave calculations relating to upper-level frontogenesis quit around a time roughly equivalent to day 8 in the present study, the further implications of the Shapiro effect are described for the first time here.

The formation of the upper-level cutoff cyclone is a truly integral part of the upper-level frontogenesis in the sense that, as illustrated in Fig. 18, the high-PV air that has been folded downward from the stratosphere and that is associated with the upper front flows ultimately around and collects into the three-dimen-

sional, wave-relative stagnation zone. A recent study by Bush and Peltier (1994) explores this process in some detail.

There is largely agreement among the numerical studies and the observations on the basic flow structure of the upper front. In our opinion, the main point of divergence is in the *methods* of analysis (and not necessarily that authors have come to physically incompatible conclusions). There are two issues we would like to comment on here: flow curvature and the nature of the feedback mechanism.

There is a school of thought that holds that the flow curvature must be accounted for to understand the pattern of upper-level divergence in the wave. These effects of flow curvature are studied through the gradient–wind relation with certain ad hoc assumptions [see Keyser and Shapiro (1986), section 4b]. As one can see by comparing Figs. 12 and 13, it is easy to locate the places and general distribution of the sinking motion over the entire wave by inspection of the Q vectors, even in a flow with significant curvature. From this we conclude that, at least to a first approximation, curvature effects are included in QG theory and are accounted for in our analysis (see the discussion of this point by KSD, p. 704).

Mudrick (1974) introduced the idea that upper-level (as well as surface) frontogenesis involves a feedback between geostrophic and ageostrophic effects. There have evolved two different readings of the Mudrick idea. The first reading [Bluestein (1993), chapter 2.6.2] says that the Mudrick idea is a pre-Q vector version of the reasoning adopted here — namely, geostrophically induced change to $\nabla_H \theta \rightarrow$ ageostrophic motion $\rightarrow$ net frontogenesis.[7] The second (and we would judge more literally accurate) reading of Mudrick (1974) is that a more general derivation of the ω equation indicates that cross-front ageostrophic motion can induce vertical velocity (see Hines and Mechoso 1991). This idea is not necessarily wrong, but the proper analytical context for its evaluation is not available. Without a well-founded balance approximation in place (e.g., geostrophy or cross-front geostrophy), a "generalized ω equation" is essentially a manipulation of the governing equations, with no clear rationale for distinguishing forcing from response.

5. Summary of the salient points

The analysis program of Hoskins (1982) applied to primitive equation simulations of evolving baroclinic waves allows one to exploit the insights of the semi-

---

[7] Mudrick (1974) interpreted his results in terms of vorticity advection, instead of the Q vector; the terms giving rise to the divergence of Q in the present case include both vorticity and thermal advection effects (see Hoskins et al. 1978).

TABLE 2. Analysis of frontogenesis following the air parcels shown in Fig. 21. Units of $\mathscr{F}$ are $(K/100 \text{ km})^2/10^5 \text{s}$, and the $|\nabla_H \theta|$ are given in K/100 km.

Day	$\mathscr{F}_g$	$\mathscr{F}_a$	$\mathscr{F}_{tilt}$	$\mathscr{F}$	$|\nabla_H \theta|_{calc}$	$|\nabla_H \theta|_{model}$
A						
7.500	5	6	8	19	2.7	2.7
7.625	8	8	8	24	3.5	3.3
7.750	15	12	8	35	4.3	4.2
7.875	20	14	6	40	5.2	4.9
8.000	24	14	7	45	6.0	5.6
B						
7.500	−10	2	20	12	2.5	2.5
7.625	−16	3	28	15	3.0	2.7
7.750	−31	3	47	19	3.6	3.6
7.875	−47	−3	114	64	4.7	4.8
8.000	15	−5	105	115	6.4	5.4
C						
7.500	−7	0	36	29	2.9	2.9
7.625	1	−12	54	43	4.1	3.9
7.750	20	−54	85	51	5.2	5.2
7.875	82	−82	72	72	6.4	5.5
8.000	100	−80	13	33	7.2	5.3

geostrophic theory while retaining primitive equation accuracy in the solutions that are analyzed.

We have revisited the canonical case study of a constant-potential-vorticity jet under a rigid lid studied earlier using a semigeostrophic equation set (Hoskins and West 1979). In our previous study (SSR) we showed that, compared with the SG model, the PE model produces a much stronger NW–SE tilt of the most unstable wave. Here we have explored the implications that this modal tilt has for the embedded frontogenesis. One salient point is that the NW–SE tilt of the mode gives rise to strong Q vector convergence along a NW–SE line just east of the surface low. The implied horizontal ageostrophic flow convergence reinforces the geostrophic, and a positive feedback is demonstrated. This process leads to the early formation of the feature identified as the warm front in many studies of this type.

The other canonical study relating to upper-level frontogenesis is the semigeostrophic modeling study of Heckley and Hoskins (1982), where the upper lid is removed in favor of a constant-potential-vorticity stratosphere. Following the development of the unstable baroclinic wave that grows in this base state with our PE model leads us to identify several new facets of upper-level frontogenesis and its relation to the development of the upper-level "cutoff" cyclone: The phase lag of the temperature wave with respect to the geopotential wave at the level of upper-frontogenesis is identified as a consequence of the finite-amplitude wave development, rather than part of the cause. The pattern of temperature and geopotential implies strong downward motion for the reasons explored by Shapiro (1981) and Keyser and Pecnick (1985). Finally, we observe here that the latter mechanism implies a fur-

ther three-dimensionalization of the flow, contributing to the formation of the cutoff cyclone just downstream from the upper-level front.

Several areas are currently being pursued. At the current grid resolution, there is no sign of unbalanced motion (gravity waves) developing at any point of the development. One would expect [e.g., see Snyder et al. (1993) and references] that such imbalance would develop with the smaller-scale and faster motions in evidence by day 9. We are conducting higher-resolution studies to investigate the nature of the imbalances should they occur. Beyond this we anticipate experiments where the effects of surface friction and resolved clouds on the motion are included.

APPENDIX

Flexible Tropopause Base State

The base state with constant PV in the troposphere and another constant, but larger, value in the stratosphere is found by solving the nonlinear PV equation for ϕ:

$$PV = (f + f^{-1}\phi_{yy}) \frac{\theta_0}{g} \phi_{zz} - \frac{\theta_0}{fg} \phi_{yz}^2, \quad (A1)$$

and recovering the velocity and potential temperature using

$$fu = -\phi_y \quad (A2)$$

and

$$\theta = \frac{\theta_0}{g} \phi_z. \quad (A3)$$

The solution procedure for $y \in (0, y_L)$ and $z \in (0, H)$ is to specify PV and solve (A1) using a nonlinear SOR technique with Dirichlet boundary conditions at the $z = 0$ and $y = 0, y_L$ boundaries and Neumann boundary conditions at $z = H$. The Neumann condition is $\phi_z(y, H) = C_\phi$, where C_ϕ is a specified constant. The Dirichlet conditions are derived as follows. The velocity u is set to zero along the $z = 0$ boundary. From (A2), ϕ is constant along the lower boundary ($z = 0$) and is set equal to a constant ϕ_0. For the lateral boundaries we require that

$$PV = \frac{f\theta_0}{g} \phi_{zz}, $$

which is solved at the $y = 0, y_L$ boundaries using the Neumann condition at the upper boundary and the Dirichlet condition at the lower boundary.

An analytical formula is used to specify PV such that it closely resembles that used in the HH jet. Given tropospheric and stratospheric PV, PV_t, and PV_s, respec-

tively, the equation for PV in $y \in (0, y_L)$ and $z \in (0, H)$ is

$$PV = \frac{PV_s + PV_t}{2}$$

$$- \left(\frac{PV_s - PV_t}{2}\right) \tanh\left(\frac{2.65(z - z_{tp}(y))}{\Delta z_{tr}}\right),$$

where z_{tr} is a scale for the thickness of the tropopause, and $z_{tp}(y)$ is the tropopause height, specified as

$$z_{tp} = z_m - \Delta z_e \tanh\left(\frac{2.65(y - y_L/2)}{\Delta y_e}\right)$$

$$+ \Delta z_{es} \tanh\left(\frac{2.65(y - y_L/4)}{2\Delta y_e}\right)$$

$$+ \Delta z_{es} \tanh\left(\frac{2.65(y - 3y_L/4)}{2\Delta y_e}\right),$$

where z_m is the tropopause height in the center of the domain $(y = y_L/2)$, Δz_e is the maximum vertical displacement from z_m of the tropopause north and south of the jet, Δz_{es} is the tropopause displacement needed to produce the quiescent zones in the velocity field by the northern and southern boundaries, and y_e is a scale for the horizontal extent for the sloping tropopause regions.

Parameter values used to reproduce (as best we could judge from their Fig. 4) the HH jet (the 30 m s^{-1} jet) are

$$PV_s = 2.4 \text{ PVU}, \quad PV_t = 0.4 \text{ PVU}, \quad z_m = 8775 \text{ m},$$

$$\Delta z_{tr} = 250 \text{ m}, \quad \Delta z_e = 1275 \text{ m}, \quad \Delta z_{es} = 382.5 \text{ m},$$

$$\Delta y_e = 600 \text{ km}, \quad C_\phi = 11.772 \text{ m s}^{-2},$$

and

$$\phi_0 = 10^4 \text{ m}^2 \text{ s}^{-2} \text{ K}.$$

For HH70 (the 70 m s^{-1} jet), the parameters PV_s, z_e, and z_{es} are multiplied by 1.5, resulting in

$$PV_s = 3.6 \text{ PVU}, \quad \Delta z_e = 1912.5 \text{ m}, \quad \Delta z_{es} = 574 \text{ m}.$$

REFERENCES

Bluestein, H. B., 1993: Synoptic–Dynamic Meteorology in Midlatitudes. Vol. II. Oxford University Press, 594 pp.

Bush, A. B. G., and W. R. Peltier, 1994: Tropopause folds and synoptic-scale baroclinic wave life cycles. J. Atmos. Sci., 51, 1581–1604.

Buzzi, A., T. Nanni, and M. Tagliazucca, 1977: Mid-tropospheric frontal zones: Numerical experiments with an isentropic coordinate primitive equation model. Arch. Meteor. Geophys. Bioklim., A26, 155–178.

Cooper, I. M., A. J. Thorpe, and C. H. Bishop, 1992: The role of diffusive effects on potential vorticity in fronts. Quart. J. Roy. Meteor. Soc., 118, 620–647.

Davies, H. C., C. Scähr, and H. Wernli, 1991: The palette of fronts and cyclones within a baroclinic wave development. J. Atmos. Sci., 48, 1666–1689.

Davies-Jones, R., 1991: The frontogenetical forcing of secondary circulation. Part I: The duality and generalization of the Q vector. J. Atmos. Sci., 48, 497–509.

Heckley, W. A., and B. J. Hoskins, 1982: Baroclinic waves and frontogenesis in a nonuniform potential vorticity semi-geostrophic model. J. Atmos. Sci., 39, 1999–2016.

Held, I. M., and D. G. Andrews, 1983: On the direction of the eddy momentum flux in baroclinic instability. J. Atmos. Sci., 40, 2220–2231.

Hines, K. M., and C. R. Mechoso, 1991: Frontogenesis processes in the middle and upper troposphere. Mon. Wea. Rev., 119, 1225–1241.

——, and ——, 1993: Influence of surface drag on the evolution of fronts. Mon. Wea. Rev., 121, 1152–1175.

Hoskins, B. J., 1982: The mathematical theory of frontogenesis. Ann. Rev. Fluid Mech., 14, 131–151.

——, and F. P. Bretherton, 1972: Atmospheric frontogenesis models: Mathematical formulation and solution. J. Atmos. Sci., 29, 11–37.

——, and N. V. West, 1979: Baroclinic waves and frontogenesis. Part II: Uniform potential vorticity jet flows—cold and warm fronts. J. Atmos. Sci., 36, 1663–1680.

——, I. Draghici, and H. C. Davies, 1978: A new look at the ω-equation. Quart. J. Roy. Meteor. Soc., 104, 31–38.

——, M. E. McIntyre, and A. W. Robertson, 1985: On the use and significance of isentropic potential-vorticity maps. Quart. J. Roy. Meteor. Soc., 111, 877–946.

Keyser, D., and M. J. Pecnick, 1985: A two-dimensional model primitive equation model of frontogenesis forced by confluence and horizontal shear. J. Atmos. Sci., 42, 1259–1282.

——, and M. A. Shapiro, 1986: A review of the structure and dynamics of upper-level frontal zones. Mon. Wea. Rev., 114, 452–499.

——, and R. Rotunno, 1990: On the formation of potential vorticity anomalies in upper-level jet-front systems. Mon. Wea. Rev., 118, 1914–1921.

——, M. J. Reeder, and R. J. Reed, 1988: A generalization of Petterssen's frontogenesis function and its relation to the forcing of vertical motion. Mon. Wea. Rev., 116, 762–780.

——, B. D. Schmidt, and D. G. Duffy, 1989: A technique for representing three-dimensional vertical circulations in baroclinic disturbances. Mon. Wea. Rev., 117, 2463–2494.

——, ——, and ——, 1992: Quasigeostrophic diagnosis of three-dimensional ageostrophic circulations in an idealized baroclinic disturbance. Mon. Wea. Rev., 120, 698–730.

McWilliams, J. C., and P. R. Gent, 1980: Intermediate models of planetary circulations in the atmosphere and ocean. J. Atmos. Sci., 37, 1657–1678.

Mudrick, S. E., 1974: A numerical study of frontogenesis. J. Atmos. Sci., 31, 869–892.

Nakamura, N., 1993: Momentum flux, flow symmetry, and the nonlinear barotropic governor. J. Atmos. Sci., 50, 2159–2179.

Newton, C. W., and A. Trevisan, 1984: Clinogenesis and frontogenesis in jet-stream waves. Part II: Channel model numerical experiments. J. Atmos. Sci., 41, 2717–2734.

Polavarapu, S. M., and W. R. Peltier, 1990: The structure and nonlinear evolution of synoptic scale cyclones: Life cycle simulations with a cloud-scale model. J. Atmos. Sci., 47, 2645–2672.

Rivest, C., C. A. Davis, and B. F. Farrell, 1992: Upper-tropospheric synoptic-scale waves. Part I: Maintenance as Eady normal modes. J. Atmos. Sci., 49, 2108–2119.

Sanders, F., L. F. Bosart, and C.-C. Lai, 1991: Initiation and evolution of an intense upper-level front. Mon. Wea. Rev., 119, 1337–1367.

Schär, Ch., and H. Wernli, 1993: Structure and evolution of an isolated semi-geostrophic cyclone. Quart. J. Roy. Meteor. Soc., 119, 57–90.

Shapiro, M. A., 1975: Simulation of upper-level frontogenesis with

a 20-level isentropic coordinate primitive equation model. *Mon. Wea. Rev.,* **103,** 591–604.

——, 1981: Frontogenesis and geostrophically forced secondary circulations in the vicinity of jet stream-frontal zone systems. *J. Atmos. Sci.,* **38,** 954–973.

——, and D. Keyser, 1990: Fronts, jet streams and the tropopause. *Extratropical Cyclones. The Erik Palmén Memorial Volume,* C. Newton and E. O. Holopainen, Eds., Amer. Meteor. Soc., Chapter 10, 262 pp.

Snyder, C., W. C. Skamarock, and R. Rotunno, 1991: A comparison of primitive-equation and semigeostrophic simulations of baroclinic waves. *J. Atmos. Sci.,* **48,** 2179–2194.

——, ——, and ——, 1993: Frontal dynamics near and following frontal collapse. *J. Atmos. Sci.,* **50,** 3194–3212.

Takayabu, I., 1986: Roles of the horizontal advection on the formation of surface fronts and on the occlusion of a cyclone developing in a baroclinic westerly jet. *J. Meteor. Soc. Japan,* **64,** 329–345.

Thorncroft, C. D., B. J. Hoskins, and M. E. McIntyre, 1993: Two paradigms of baroclinic-wave life-cycle behavior. *Quart. J. Roy. Meteor. Soc.,* **119,** 17–55.

Whitaker, J. S., and C. Snyder, 1993: The effects of spherical geometry on the evolution of baroclinic waves. *J. Atmos. Sci.,* **50,** 597–612.